



# Numerical simulations of flow around three cylinders using momentum exchange-based immersed boundary-lattice Boltzmann method

Rongyang Wang <sup>a,c</sup>, Yanhu He <sup>a,c</sup>, Liqun Chen <sup>a,c</sup>, Yingpeng Zhu <sup>b</sup>, Yikun Wei <sup>b,\*</sup>

<sup>a</sup> College of Mechanical and Electrical Engineering, Huzhou Vocational and Technical College, Huzhou, 313000, China

<sup>b</sup> Faculty of Mechanical Engineering and Automation, Zhejiang Sci-Tech University, Hangzhou, 310018, China

<sup>c</sup> Key Laboratory of Robot System Integration and Intelligent Equipment of Huzhou City, Huzhou, 313000, China

## ARTICLE INFO

### Keywords:

Staggered cylinders  
IB-LBM  
Flow interference  
Drag and lift forces  
Vortex dynamics  
Fluid-structure interaction

## ABSTRACT

Wake flow behind multiple bluff bodies is of critical significance in ocean engineering and has important scientific significance in fluid mechanics and dynamics. Three cylinders arranged in side-by-side, tandem, equilateral-triangular, and staggered arrangements were extensively researched in the previous study. In this study, the flow passing through three cylinders in staggered and equilateral-triangular arrangement were numerical calculated using a momentum exchange-based immersed boundary-lattice Boltzmann method. The numerical investigations for staggered arrangement were carried out by changing the Reynolds number ( $Re$ ) from 10 to 200 with an increment of 1, and varying the gap ratio ( $\delta = \Delta P/D$ ) from 0.1 to 8.0 with an increment of 0.1. The flow patterns of three equilateral-triangular cylinders with different gap ratios at  $Re = 100$  were also numerically studied. The numerical results identified various flow patterns, and the variations of the above two parameters have a decisive influence on the vortex shedding patterns and flow properties. The drag coefficient, lift coefficient, and Strouhal number ( $St$ ) were also surveyed to demonstrate the relationship among flow pattern, parameters  $\delta$  and  $Re$ . The outcomes in this paper provide a relatively comprehensive understanding to the vortex shedding patterns and flow properties of three circular cylinders with different gap ratios and Reynolds number.

## 1. Introduction

Flow around bluff bodies is a subject with important research value in various engineering applications, including offshore drilling platforms, offshore wind farms, cross-sea bridges, suspension bridges, heat exchangers, and skyscrapers (Tu et al., 2020; Ma et al., 2018), it also has critical significance in practical engineering and important scientific significance in fluid mechanics and dynamics. There are four typical arrangements of three cylinders, such as side-by-side, tandem, equilateral-triangular, and staggered, as shown in Fig. 1. Zhou et al. (2021) noted that the tandem and side-by-side arrangements are two special cases of three staggered cylinders, the staggered arrangement is the extremely common pattern and has universal significance. It is a well-known fact that the triangle is a more solid arrangement, in practical applications of offshore engineering, like the building of floating wind farm. Therefore, this paper mainly focuses on the Reynolds ( $Re$ ) number and gap ratio ( $\delta$ ) on the wake flow patterns, force coefficients, and Strouhal ( $St$ ) number in triangular and staggered arrangement.

Many scholars have conducted a series of studies on the flow passed

through two cylinders with different gap ratios,  $Re$  values, and arrangements (Bai et al., 2020; Shui et al., 2021; Deng et al., 2006; Wang et al., 2010). Ma et al. (2017), Kang (2003), and Zhou et al. (2021) investigated the effect of gap ratios and  $Re$  on the wake flow patterns for two side-by-side cylinders. It's also reported that the single cylinder's vortex shedding frequency is smaller than that of two-cylinders. Shui et al. (2021) defined the two-layered and secondary vortex formation and found the flow parameters notably jump in the range  $4.4 \leq \delta \leq 4.5$  for the flow around two tandem cylinders. Wang et al. (2010) experimentally investigated two circular cylinders in tandem arrangement at low  $Re$  using a high-speed camera and spatiotemporal evolution method, which found that there is a secondary vortex street phenomenon in the wake flow. Hu and Zhou (2008) and Alam et al. (2016) experimentally studied the wake flow structure,  $St$ , and force coefficients of two staggered cylinders, four distinct flow patterns were observed. For the flow around three cylinders, it is critical to investigate whether the flow characteristics are the same as those of two cylinders, or whether some new characteristics emerge.

Some numerical and experimental studies on the flow around three

\* Corresponding author.

E-mail address: [yikunwei@zstu.edu.cn](mailto:yikunwei@zstu.edu.cn) (Y. Wei).

cylinders have been executed. Islam et al. (2016), Vassel-Be-Hagh et al. (2013), and Abbasi et al. (2018a,b) investigated the wake flow patterns, drag coefficients, lift coefficients, and velocity characteristics for three cylinders arranged in side-by-side and tandem. Six distinguished flow patterns were defined by Islam et al. (2018) for the flow past three tandem cylinders. Abbasi et al. (2018a,b) pointed out that the shear layers can be classified as four major trends for unequal gap spacings, and suitable unequal gap spacing combinations can restrain the flow-induced forces for the flow pass through three cylinders in tandem arrangement. Gao et al. (2019) indicated that flow past three cylinders in an equilateral-triangle arrangement is more complicated than that in side-by-side and tandem arrangements. The particle image velocimetry technique and Piezoelectric load cells were used by Yang et al. (2020) to experimentally investigated the effects of gap ratio and array orientation of flow at fixed  $Re$  of 8000 for flow past three cylinders in equilateral-triangular arrangement. It is concluded that  $Re$ , gap ratio, arrangement mode, and flow velocities significantly influence the wake flow patterns, force coefficients, and Strouhal number. Based on previous studies, it is possible to master the flow characteristics of three-cylinder arrangement in Fig. 1 (a)–(c). However, the attention paid to flow around three staggered arrangement cylinders (Fig. 1d) are insufficient and worthy of further study.

This study systematically investigated the characteristics of three cylinders in triangular and staggered arrangement with the main aim of answering the following two questions: (I) How  $Re$  and  $\delta$  effect on the transition of flow patterns and force characteristics? (II) How will the force coefficients and shedding frequency change with  $\delta$  at low  $Re$ ? The overall structure of this article is as follows. The problem description, boundary conditions, governing equations, and numerical methodology are presented in Section 2. The grid independence and code validation are described in Section 3. The wake flow patterns, force coefficients, and Strouhal number ( $St$ ) are discussed in Section 4. The Section 5 part gives the conclusions of this paper.

## 2. Numerical methodology

### 2.1. Problem description and boundary conditions

Fig. 2 illustrates the computational domain, where three identical staggered circular cylinders, named Cylinder 1, Cylinder 2, and Cylinder 3 (C1, C2, and C3, respectively), are placed in the computing domain, and the angle  $\theta$  between the staggered cylinders and  $x$  direction is 45°. The gap ratio  $\delta$  for staggered arrangements,  $\delta = \Delta P/D$ , varies from 0.1 to 8.0 with increments of 0.1. The gap ratio  $\delta$  for three equilateral-triangular cylinders are 0.4, 3.0 and 6.0. The computational domain consists of  $1200 \times 1000$  points ( $L_x \times L_y = 60D \times 50D$ ), where  $D = 20$  is the diameter of the circular cylinder. The staggered arrangements cylinder C2 and equilateral-triangular arrangements C1 are located  $10D$  downstream of the inlet boundary and center in the transverse direction. West and Apelt (1997) demonstrated that the drag is unaffected by the blockage ratio ( $D/L_y$ ) because the blockage ratio (2%) for a single

cylinder is less than the critical value of 6%.  $x$  and  $y$  are the Cartesian coordinates along the streamwise and transverse directions, respectively. The computations were performed for a variable  $Re = U_\infty D/\mu$ , where  $U_\infty$  and  $\mu$  are the freestream velocity and fluid viscosity, respectively.

### 2.2. Governing equations

First, it is assumed that the fluid is Newtonian and viscous incompressible, flows in a two-dimensional (2D) domain  $\Omega$ , as shown in Fig. 2 (a), containing an immersed boundary of  $\Gamma$ , as shown in Fig. 3. The equations governing the fluid flow can be modeled with the conservation of mass and momentum equations of the immersed boundary method, defined as Eq. (1)–(5) (Wu and Shu, 2009). The Navier-Stokes equations of mass and momentum with a force density  $\vec{f}$  are described in by Eqs. (1) and (2), the interaction between the fluid flow and immersed boundary is described by Eqs. (3) and (4), and Eq. (5) defines the boundary force on a cylinder.

$$\nabla \cdot \vec{u} = 0 \quad (1)$$

$$\rho \left( \frac{\partial \vec{u}}{\partial t} + \vec{u} \cdot \nabla \vec{u} \right) + \nabla p = \nu \Delta \vec{u} + \vec{f} \quad (2)$$

$$\vec{f}(\vec{x}, t) = \int_{\Gamma} \vec{F}(s, t) \delta(\vec{x} - \vec{X}(s, t)) ds \quad (3)$$

$$\frac{\partial \vec{X}(s, t)}{\partial t} = \vec{u}(\vec{X}(s, t), t) = \int_{\Omega} \vec{u}(\vec{x}, t) \delta(\vec{x} - \vec{X}(s, t)) d\vec{x} \quad (4)$$

$$\vec{F}(s, t) = \vec{S}(\vec{X}(s, t), t) \quad (5)$$

where  $p$ ,  $\vec{u}$ ,  $\rho$ ,  $\nu$ ,  $\vec{x}$ ,  $\vec{f}$ ,  $\vec{X}$ , and  $\vec{F}$  are the fluid pressure, fluid velocity, fluid density, kinematic viscosity, Eulerian coordinates, fluid phase force density, Lagrangian coordinates, and boundary force density, respectively. The velocity  $\vec{u}$  is a vector field with  $u$  and  $v$  as components in the  $x$  and  $y$  directions, respectively.  $\delta(\vec{x} - \vec{X}(s, t))$  denotes the Dirac delta function.

### 2.3. Momentum exchange-based immersed boundary-lattice Boltzmann method

For the momentum exchange-based IB-LBM, unlike the direct forcing scheme and penalty approach, the interaction force between the fluid and structure is simply calculated by the momentum exchanged method, which is more physically plausible and does not bring in any user-defined parameters. The two-dimensional lattice Boltzmann equation (LBE) is used to represent Eqs. (1) and (2), and the 2D and nine-lattice velocities (D2Q9) model is used (Qian et al., 1992), as shown in Fig. 4, where the particle velocities are defined as.

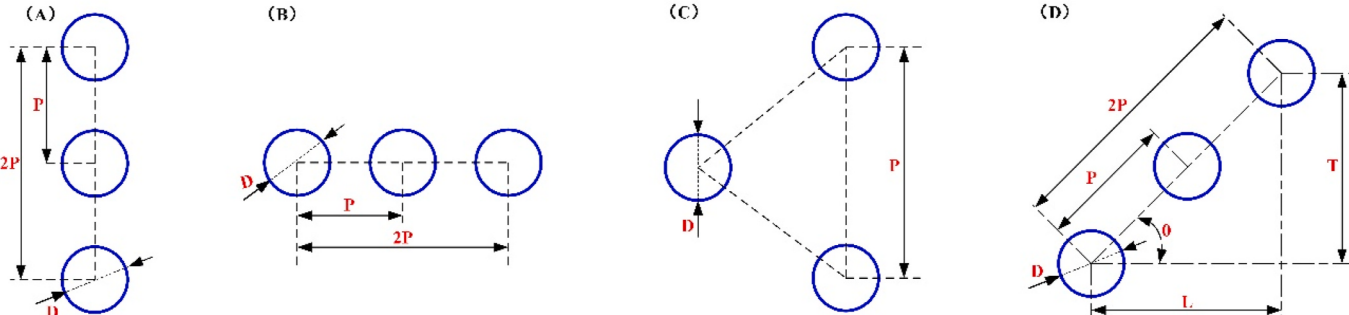


Fig. 1. Schematic diagrams of different arrangements: (a) side-by-side, (b) tandem, (c) triangular, and (d) staggered.

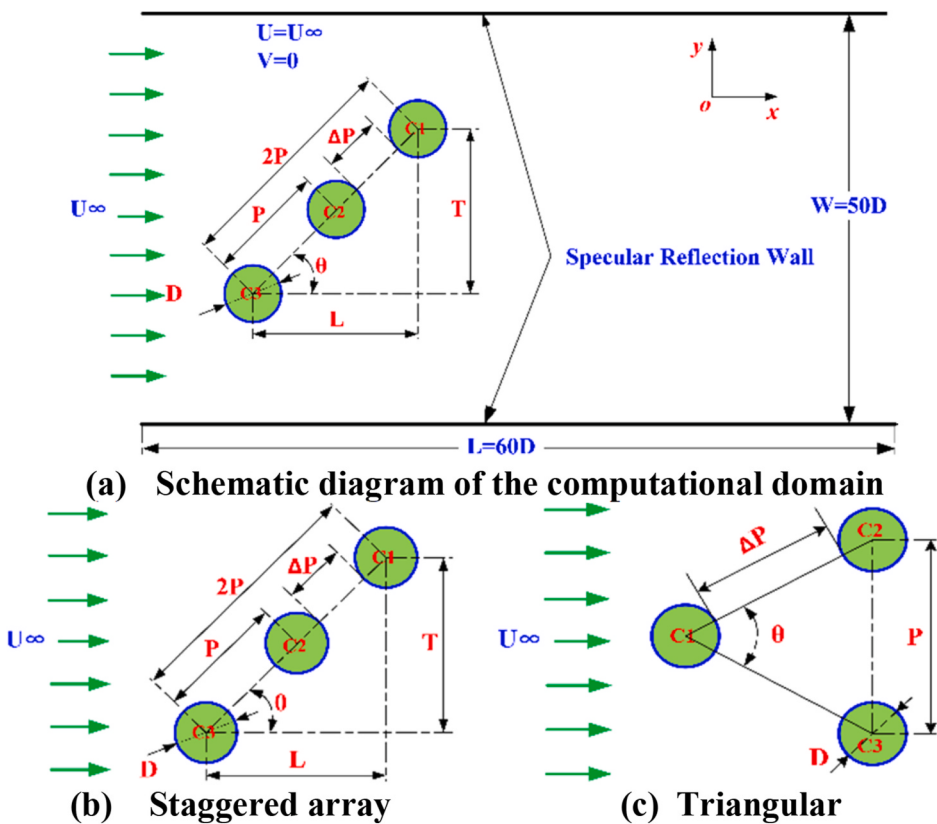


Fig. 2. Arrangement and computational domain for three cylinders.

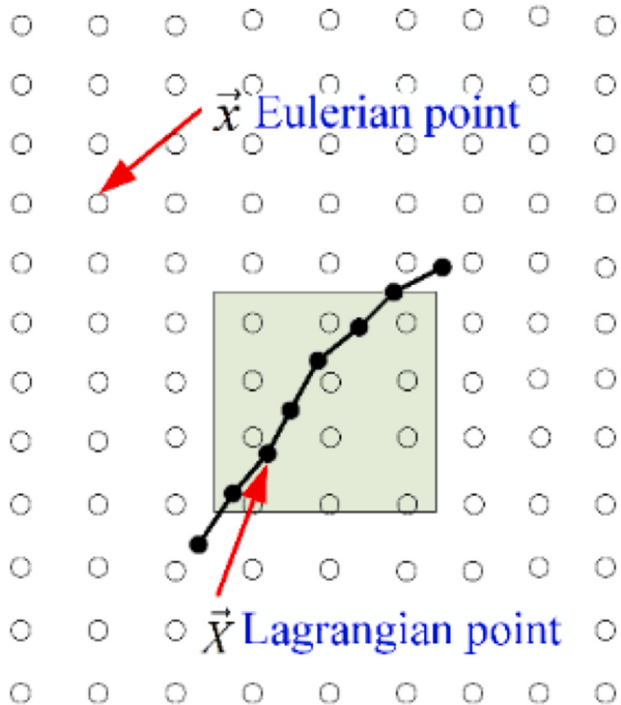


Fig. 3. Schematic diagram of the immersed boundary.

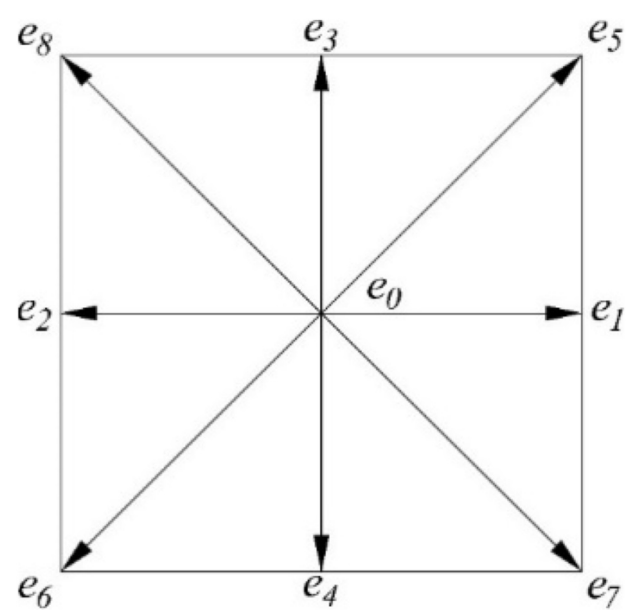


Fig. 4. Schematic diagram of the immersed boundary.

$$\vec{e}_\alpha = \begin{cases} 0 & \alpha=0 \\ c \times (\cos[(\alpha-1)\pi/2], \sin[(\alpha-1)\pi/2]) & \alpha=1,2,3,4 \\ \sqrt{2}c \times (\cos[(\alpha-5)\pi/2+\pi/4], \sin[(\alpha-5)\pi/2+\pi/4]) & \alpha=5,6,7,8 \end{cases} \quad (6)$$

here,  $c = \delta x / \delta t$ , where  $\delta x$  and  $\delta t$  are the lattice spacing between two successive nodes and the time step, respectively.

The fluid kinetics governed by the LBM with an external force term can be described as

$$f_a(\vec{x} + \vec{e}_\alpha \delta t, t + \delta t) - f_a(\vec{x}, t) = -\frac{1}{\tau} (f_a(\vec{x}, t) - f_a^{eq}(\vec{x}, t)) + \vec{F}_\alpha \delta t \quad (7)$$

$$\vec{F}_\alpha = \left(1 - \frac{1}{2\tau}\right) \omega_\alpha \left( \frac{\vec{e}_\alpha - \vec{u}}{c_s^2} + \frac{\vec{e}_\alpha \cdot \vec{u}}{c_s^4} \cdot \vec{e}_\alpha \right) \cdot \vec{f} \quad (8)$$

$$\rho \vec{u} = \sum_\alpha \vec{e}_\alpha f_a + 0.5 \vec{f} \delta t \quad (9)$$

where  $\vec{f}_\alpha$  denotes the distribution function,  $\vec{f}_\alpha^{eq}$  denotes the equilibrium density distribution function,  $\vec{f}$  is the force density distributed from the boundary force, and  $\tau$  is the single relaxation parameter.  $\omega_\alpha$  are coefficients:  $\omega_0 = 4/9$ ,  $\omega_1 = \omega_2 = \omega_3 = \omega_4 = 1/9$ ,  $\omega_5 = \omega_6 = \omega_7 = \omega_8 = 1/36$ .  $\vec{u}^* = 1/\rho \sum_\alpha \vec{e}_\alpha \vec{f}_\alpha$  is the intermediate fluid velocity,  $\delta \vec{u} = 1/(2\rho)^* \vec{f} \delta t$  is the velocity correction,  $c_s = c/\sqrt{3}$ . Then, Eq. (9) can be expressed as  $\vec{u} = \vec{u}^* + \delta \vec{u}$ .

The equilibrium density distribution function is

$$f_a^{eq}(\vec{x}, t) = \rho \omega_\alpha \left[ 1 + \frac{\vec{e}_\alpha \cdot \vec{u}}{c_s^2} + \frac{(\vec{e}_\alpha \cdot \vec{u})^2 - (c_s |\vec{u}|^2)}{2c_s^4} \right] \quad (10)$$

The Dirac delta function  $\delta(\cdot)$  is smoothly approximated by  $D_{ij}$ :

$$D_{ij}(\vec{x}_{ij} - \vec{X}_\Gamma) = \frac{1}{h^2} \delta_h \left( \frac{x - X_\Gamma}{h} \right) \delta_h \left( \frac{y - Y_\Gamma}{h} \right) \quad (11)$$

$$\delta(r) = \begin{cases} \frac{1}{4} (1 + \cos(\pi|r|/2)) & |r| \leq 2 \\ 0 & |r| > 2 \end{cases} \quad (12)$$

The immersed boundary equations (13)-(15) are used to represent Eqs. (3) and (4):

$$\delta \vec{u}(\vec{x}_{ij}, t) = \sum_l \delta \vec{u}_B^l(\vec{X}_B^l, t) D_{ij}(\vec{x}_{ij} - \vec{X}_B^l) \Delta s_l \quad (l=1, 2, \dots, m) \quad (13)$$

$$\vec{U}_B(\vec{X}_B^l, t) = \sum_{ij} \vec{u}(\vec{x}_{ij}, t) D_{ij}(\vec{x}_{ij} - \vec{X}_B^l) \Delta x \Delta y \quad (l=1, 2, \dots, m) \quad (14)$$

$$\vec{f}(\vec{x}_{ij}, t) = \sum_l \vec{f}(\vec{X}_l, t) D_{ij}(\vec{x}_{ij} - \vec{X}_l) \Delta s \quad (15)$$

where  $\Delta s$  is the arc length of the boundary element.

A force density distribution function on the Lagrangian boundary point was proposed by Niu et al. (2006) based on 2D Lagrangian interpolated polynomials, which can be approximated as

$$f_a(\vec{X}_\Gamma, t) = \sum_{ij} \left( \prod_{k=1, k \neq i}^{i_{max}} \frac{X_l - x_{kj}}{x_{ij} - x_{kj}} \right) \left( \prod_{m=1, m \neq j}^{j_{max}} \frac{Y_l - y_{mj}}{y_{ij} - y_{kj}} \right) f_a(\vec{x}_{ij}, t) \quad (16)$$

where  $i_{max}$  and  $j_{max}$  represents the  $x$  direction mesh points and  $y$  direction, respectively. Eq. (5) can be approximated in all velocity directions as (Yuan et al., 2014)

$$f_a(\vec{X}_\Gamma, t) = \int f_a(\vec{x}, t) \alpha(\vec{x} - \vec{X}) d\vec{x} \quad (17)$$

Yuan et al. (2014) and Niu et al. (2006) developed a new set of distribution functions using the bounce back rules.

$$f_{-\alpha}^{new}(\vec{X}, t) = f_\alpha(\vec{X}, t) - 2\omega_\alpha \rho \frac{\vec{e}_\alpha \vec{U}(\vec{X}, t)}{c_s^2} \quad (18)$$

where  $-\alpha$  denotes the direction opposite to  $\alpha$ . The force density can then be calculated by the momentum exchange as follows:

$$\vec{F}(\vec{X}, t) = \sum_\alpha \vec{e}_\alpha [f_\alpha^{new}(\vec{X}, t) - f_\alpha(\vec{X}, t)] \quad (19)$$

### 3. Code validation and grid independence

#### 3.1. Code validation study

To validate the accuracy and reliability of our code for momentum exchange-based immersed boundary-LBM (IB-LBM), a series of numerical simulation tests were conducted for the flow around a cylinder and three cylinders. The global flow parameters considered in this study, namely, the total lift coefficient ( $C_l$ ), total drag coefficient ( $C_d$ ), and Strouhal number ( $St$ ), are expressed as follows:

$$C_d = \frac{2F_D}{\rho U^2 D} \quad (20)$$

$$C_l = \frac{2F_L}{\rho U^2 D} \quad (21)$$

$$St = \frac{f_s D}{U} \quad (22)$$

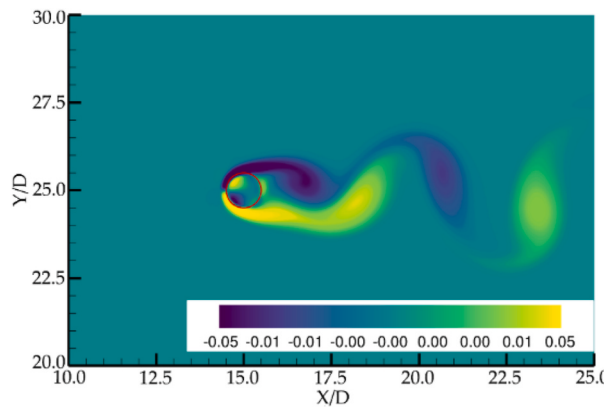
**Table 1** presents a comparison of numerical results in this paper for with experimental or numerical results from previous studies. From **Table 1**, it can be concluded that the numerical results in this paper consistent well with previously published results.

The vorticity contours and streamlines of a single cylinder at  $Re = 100$  was shown in Fig. 5. It can be clearly seen that the two types of shear layers are generated from the upper and lower sides of the cylinder, and the Karman vortex street phenomenon is also obtained in the downstream region, and the penetration of streamlines to the cylinder is obvious. All these observations agree well with those of Wu and Shu (2009), Kang and Hassan (2011), Kim et al. (2001), Lai and Peskin (2000), and Cui et al. (2017). The above-mentioned numerical calculations certificated that the momentum exchange-based IB-LBM is a feasible method to address the fluid-structure-interaction (FSI) problems. And moreover, the present results are consistent well with the previously published results, especially the experimental measurements, Yuan et al. (2014) attribute this advantage from the FSI force computed based on momentum exchange method.

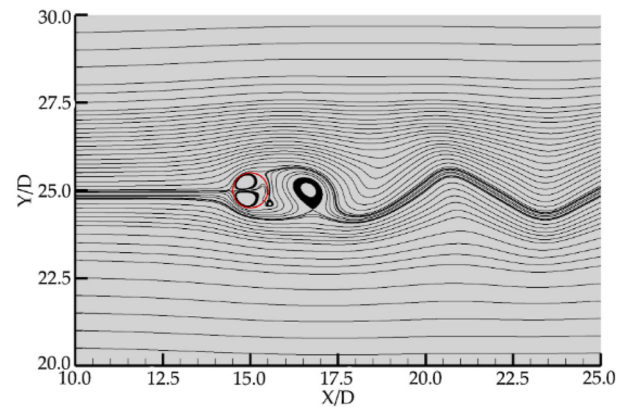
Flow pass through three tandem arrangement cylinders was also used to validate the correctness and reliability of our code. Islam et al. (2016) and Abbasi et al. (2018a,b) stated that the gap ratio can divided into three cases: narrow ( $\delta < 2.0$ ), moderate ( $2.0 < \delta < 4.0$ ), and wide ( $\delta$

**Table 1**  
Comparison of drag ( $C_d$ ) and lift ( $C_l$ ) coefficients with previous studies.

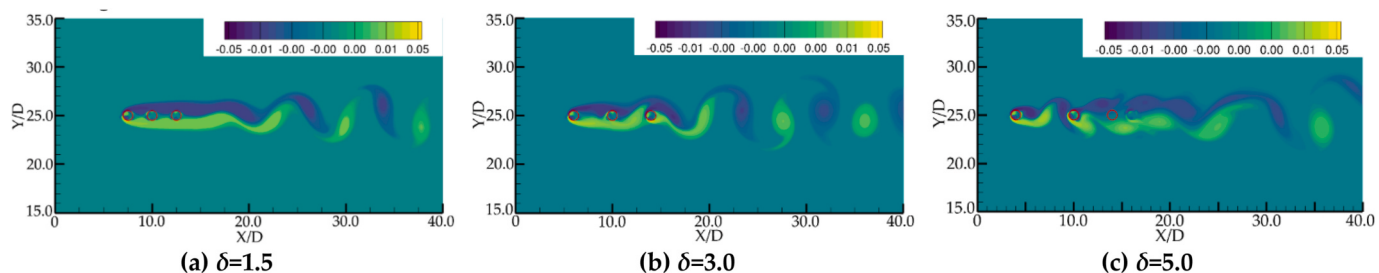
References	$C_d$	$C_l$
Wu et al.	1.364	$\pm 0.344$
Kang et al.	1.399	$\pm 0.343$
Kim et al.	1.33	$\pm 0.32$
Lai et al.	1.447	$\pm 0.33$
Cui et al.	1.358	$\pm 0.342$
Present	1.45	$\pm 0.37$



(a) Vorticity contour visualization



(b) Streamlines

Fig. 5. Vorticity contour and streamlines for the flow pass through a single circular at  $Re = 100$ .Fig. 6. Flow patterns for three staggered cylinders at  $Re = 100$ .

$> 4.0$ ) gap spacing; thus, we chose  $\delta = 1.5$ ,  $\delta = 3.0$ , and  $\delta = 5.0$  for our simulations, and the vorticity contours are described in Fig. 6. It can be demonstrated that the shear layers for  $\delta = 1.5$  move without roll up, vortices formed only in the downstream region, and the flow pattern can be defined as a single bluff body (Abbasi et al., 2018). As shown in Fig. 6 (b) that the shear layers rolled up within the gap to form vortices, and vortices formed by upstream and downstream cylinders experience an extremely complex amalgamation and disengagement in the downstream region, which is called a chaotic flow pattern.  $\delta = 5.0$  is wide enough for complete development and roll up to form vortices in the gap, however the vortices are still insignificantly restrained inside the gaps for  $\delta = 5.0$ , and the flow pattern is called alternate vortex shedding.

The time histories of drag coefficients  $C_d$  and lift coefficients  $C_l$  for three tandem arrangement cylinders with different gap ratio cases ( $\delta = 1.5$ ,  $\delta = 3.0$  and  $\delta = 5.0$ ) were described in Fig. 7. It can clearly be observed that the mean values and amplitudes of  $C_d$  and  $C_l$  are different for each cylinder. The drag coefficients ( $\delta = 1.50$ ) are approximate straight line with slight fluctuations, indicating that the drag force on each cylinder is essentially constant. The drag coefficient  $C_d$  for cylinder C2 is negative, it's may be caused by the small gap spacing trapping the flow, which pulls the middle cylinder upwards instead of pushing it downwards.

### 3.2. Grid independence study

A series of numerical simulations were conducted by representing a cylinder (diameter  $D$ ) with 80, 90, 100, 110, 120, 130, 140, 150, and 160 discrete points to validate the grid independence, where the computational domain along the longitudinal and transverse were  $60D$  and  $50D$ , respectively. The single cylinder was placed  $15D$  away from the fluid inlet and middle of the transverse boundaries. The average drag coefficient  $C_d$  and time history of the lift coefficient  $C_l$  at  $Re = 100$  under nine different discrete points condition is shown in Fig. 8 (a) and Fig. 8 (b), respectively. It can clearly be illustrated that the results for 100

discrete points are consistent enough with those for other numbers of discrete points, it's also illustrated that the average  $C_d$  is 1.4502 for 100 discrete points case and 1.4503 for 160 discrete points case, representing a deviation of approximately 0.0069%, which has little effect on the accuracy of the calculation relative to the calculation speed. Wu and Shu (2009) and Dash et al. (2014) previously used 120 Lagrangian points to represent a cylinder.

## 4. Numerical results and discussions

### 4.1. Flow patterns

#### 4.1.1. Effect of $Re$ on flow patterns

In this part, the flow patterns, fluid force, and spectral features for flow around three staggered arrangement cylinders with an inclination angle  $\theta = 45^\circ$  are presented for the range of  $Re = 10$  to  $200$  at  $\delta = 3.0$ . Intervals of  $Re = 1$  are used to reveal how the flow pattern and flow statistic sensitivity to  $Re$ . Flow pattern snapshots for cylinders in a staggered arrangement with  $\delta = 3.0$  and  $\theta = 45^\circ$  at  $Re$  ranging from 10 to 200 are depicted in Fig. 9 – 11. The behaviors of the surface lift coefficients are considered to investigate the vortex shedding frequency, the  $C_d$  and  $C_l$  according to the wake flow modes are illustrated in Figs. 9, 10 and 12. In this section, three flow patterns are considered: steady-state flow, transitional state flow, and modulation flow.

**4.1.1.1. Steady-state flow pattern.** The vorticity contours, drag coefficient  $C_d$ , and lift coefficient  $C_l$  for the steady-state wake flow pattern at  $Re = 100$ ,  $\delta = 3$ , and  $\theta = 45^\circ$  are described in Fig. 9 it can be obtained from Fig. 9 (a) that the shear layers still associated to the three cylinders in the shape of elongated recirculation bubbles in the downstream, and the vorticities shed from cylinder C2 and the gap sides of cylinder C1 and cylinder C3 are much smaller than those shedding from the upside sides of C1 and downside of C3 owing to the narrow gap spaces. As shown in Fig. 9 (b), there is no significant variation in the drag and lift coefficients

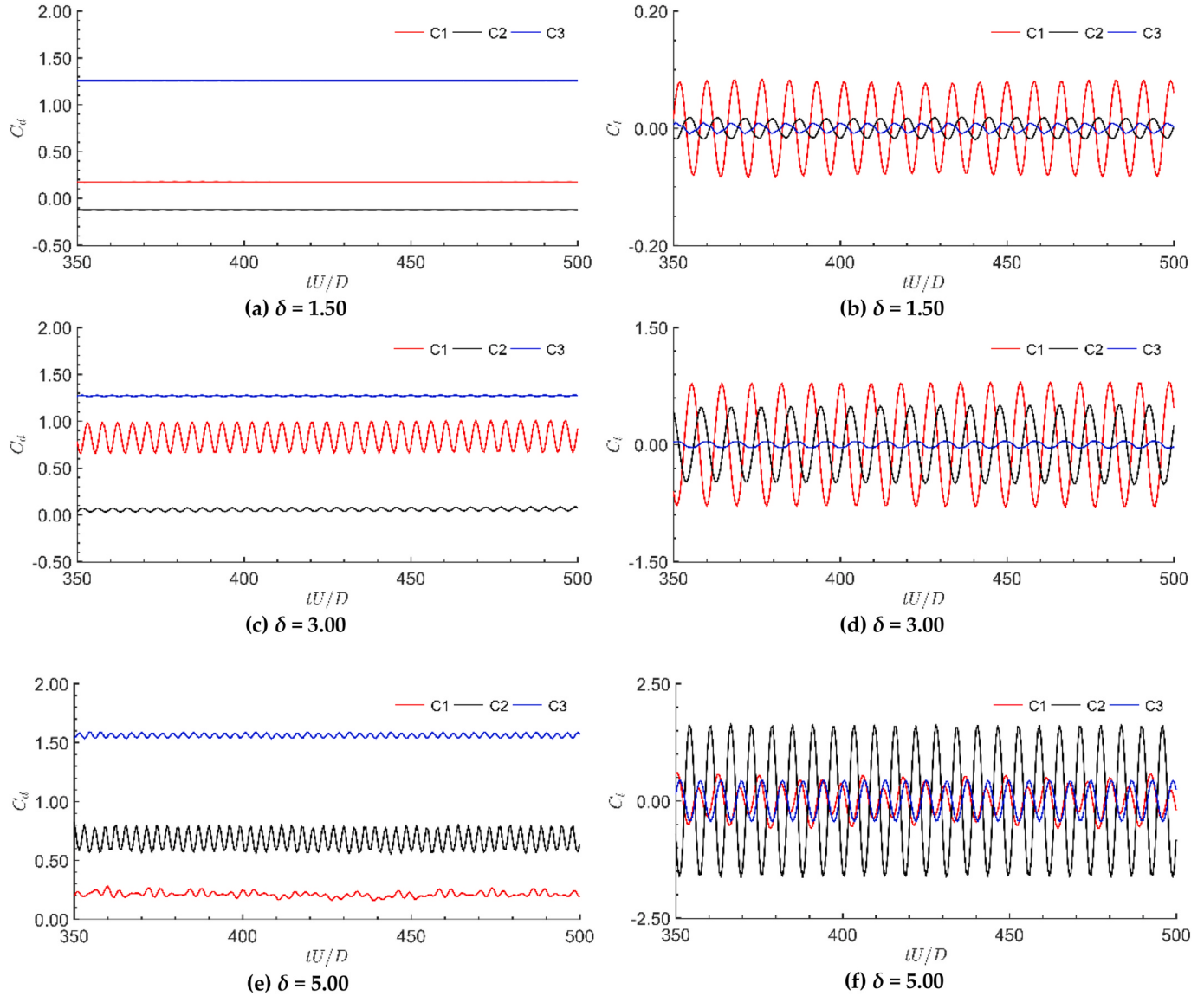


**Fig. 7.** Time histories of drag  $C_d$  and lift coefficients  $C_l$  for three tandem arrangement cylinders at  $Re = 100$ .

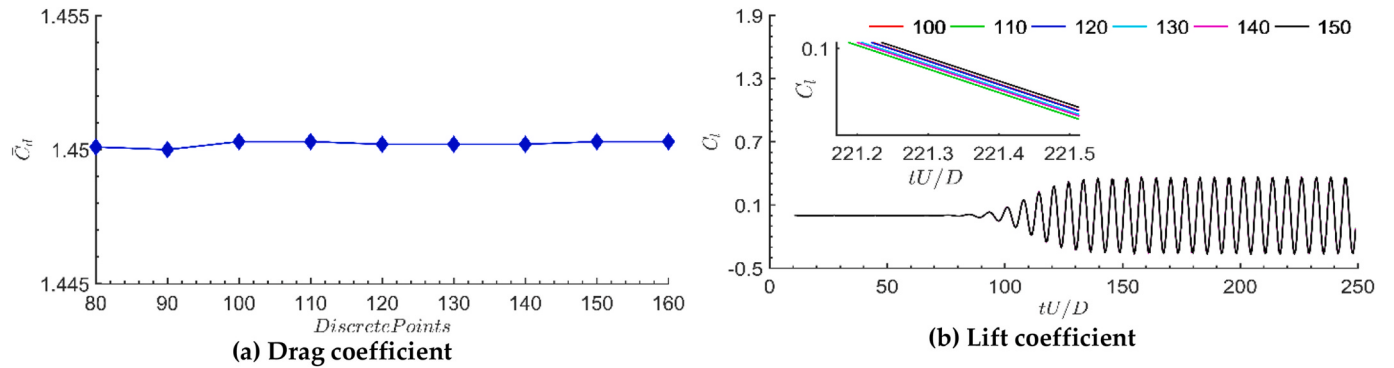


**Fig. 8.** Validation of grid independence.

with time, which confirms the steady-state flow pattern for flow around three cylinders. It was also found that the bubbles increased with  $Re$  until some unstable modes developed, and the critical  $Re$  value for the flow changing from steady-state to transitional state flow pattern is 33.

**4.1.1.2. Transitional state flow pattern.** The vorticity contours, drag coefficient  $C_d$ , and lift coefficient  $C_l$  for the transitional state flow pattern at  $Re = 100$ ,  $\delta = 3$ , and  $\theta = 45^\circ$  are shown in Fig. 10. Fig. 10 (a) shows that the shear layers remain attached to cylinder C1 in the near-wake downstream region in the form of elongated recirculation bubbles and

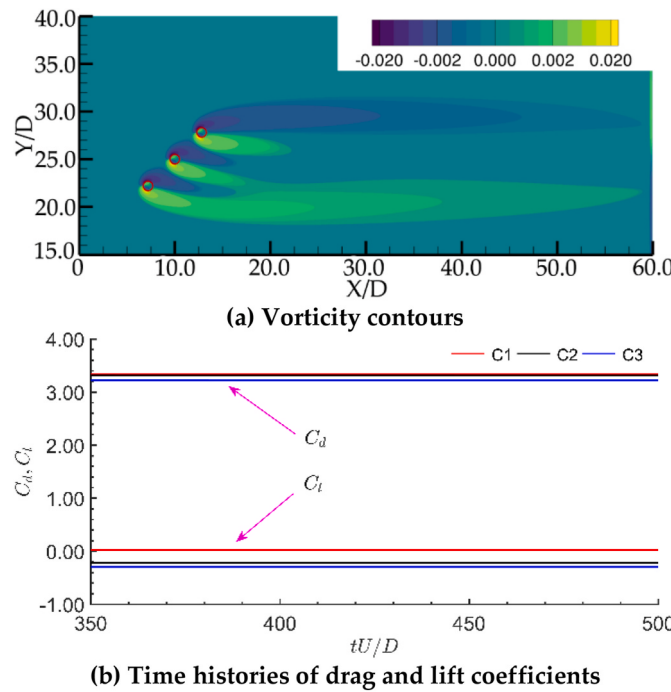


**Fig. 9.** Steady-state flow pattern of three cylinders in staggered arrangement ( $\delta = 3.0$ ,  $\theta = 45^\circ$ ) at  $Re = 10$ .

become vortices in the far-wake downstream region, while the shear layers generated from  $C_2$  and  $C_3$  remain in the elongated recirculation bubble state until the exit position of the computational domain at  $Re = 33$ . When  $Re$  reaches 50, the shear layers of  $C_3$  begin to exhibit a distinct vortex street phenomenon in the far-wake region but remain with an elongated recirculation bubble state, as shown in Fig. 10 (b). The time histories of the drag and lift coefficients shows periodic variation, which also indicates the unsteadiness phenomenon, as shown in Fig. 10 (c) and

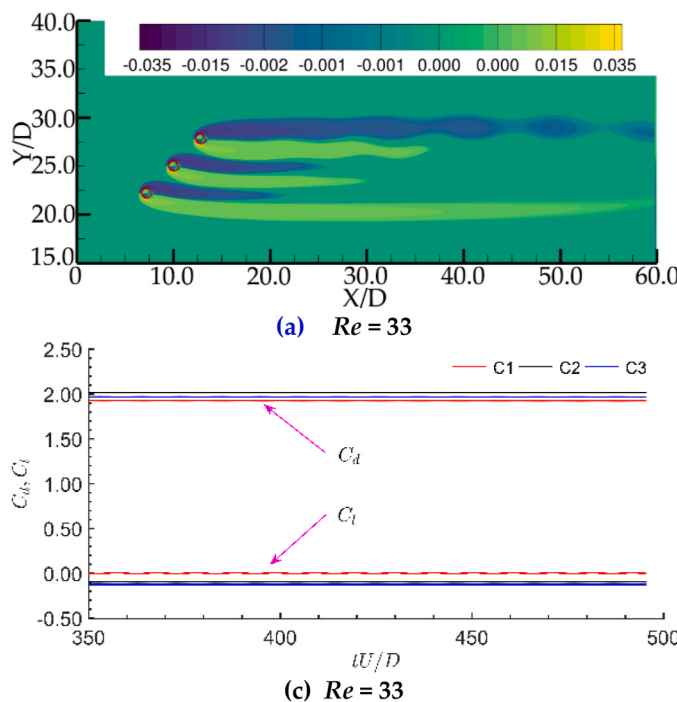


**Fig. 10.** Transitional state flow pattern of three cylinders in staggered arrangement ( $\delta = 3$ ,  $\theta = 45^\circ$ ).

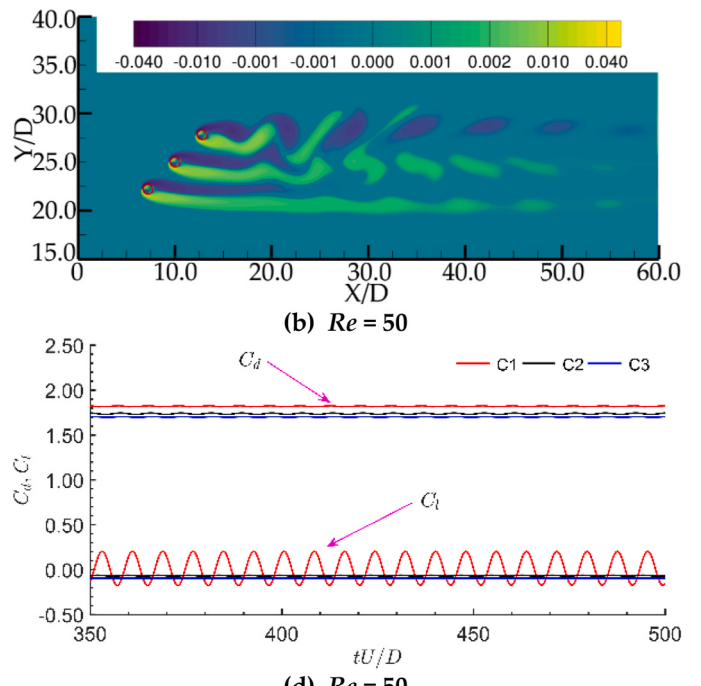
(d). The lift coefficients for transitional state flow pattern are nonlinear, and different from that in the steady-state flow pattern, which indicated that a transition for the flow pattern from a steady to unsteady state, and the  $Re$  values for the lift coefficients of  $C_1$ ,  $C_2$ , and  $C_3$  become nonlinear at 33, 40, and 50, respectively.

**4.1.1.3. Unsteady flow pattern.** The critical  $Re$  value for the onset of the complete unsteady flow pattern is 54, and representative cases of three cylinders in a staggered arrangement ( $\delta = 3$ ,  $\theta = 45^\circ$ ) at  $Re = 55$ , 100, 150, and 200 are shown in Fig. 11. It can be seen that the shed vortices are merged in the downstream region, which indicates that there is a mutual influence among the vortices in the tail flow field, and this interaction tends to decrease with an increase in  $Re$ . Furthermore, with increasing  $Re$ , the elongated recirculation bubbles of  $C_3$  in the downstream gradually decrease and form a vortex, which moves alternately.

The drag and lift coefficients for the flow pass through the three staggered arrangement cylinders ( $\delta = 3$ ,  $\theta = 45^\circ$ ) as  $Re$  varies from 55 to 200 are shown in Fig. 12. It can obviously be observed that the drag and lift coefficients demonstrate periodic behavior in stabilization stage, which indicates that the vortex has periodic shedding characteristics. The vortex shedding frequency value remains approximately the same for all three cylinders; however, there is a constant phase difference between these oscillations, i.e., they are not at their maxima simultaneously. The reason for this phenomenon is that each cylinder's vortex shedding time is inconsistent for the staggered arrangement with inclination. Unlike the transient singles of  $C_l$  and  $C_d$  for the steady-state and transitional state flow patterns, a sinusoidal variation mode with modulated frequency is observed in the unsteady flow pattern for both  $C_l$  and  $C_d$  of all three cylinders, and the modulation frequency is smaller than the vortex shedding frequency. Chatterjee et al. (2010) considered that the interaction between vortex shedding frequency and modulation frequency will produce multiple peaks in the power density spectrum analysis. Furthermore, there is a positive correlation between the amplitudes of  $C_l$  and  $Re$ , and the order from large to small is  $C_1$ ,  $C_2$ , and  $C_3$ .

#### 4.1.2. Effect of $\delta$ on wake patterns

The flow pattern snapshots, drag coefficient and lift coefficient for



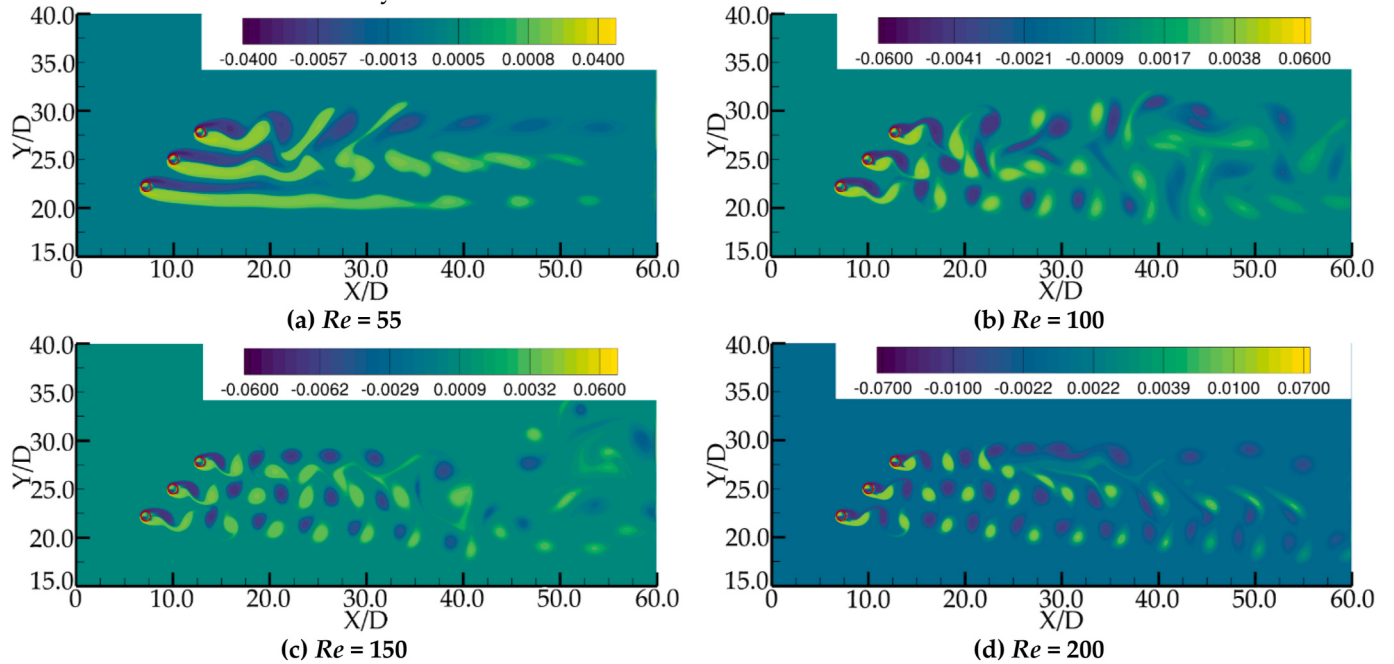


Fig. 11. Vorticity contours for three cylinders arranged in staggered arrangement ( $\delta = 3$ ,  $\theta = 45^\circ$ ).

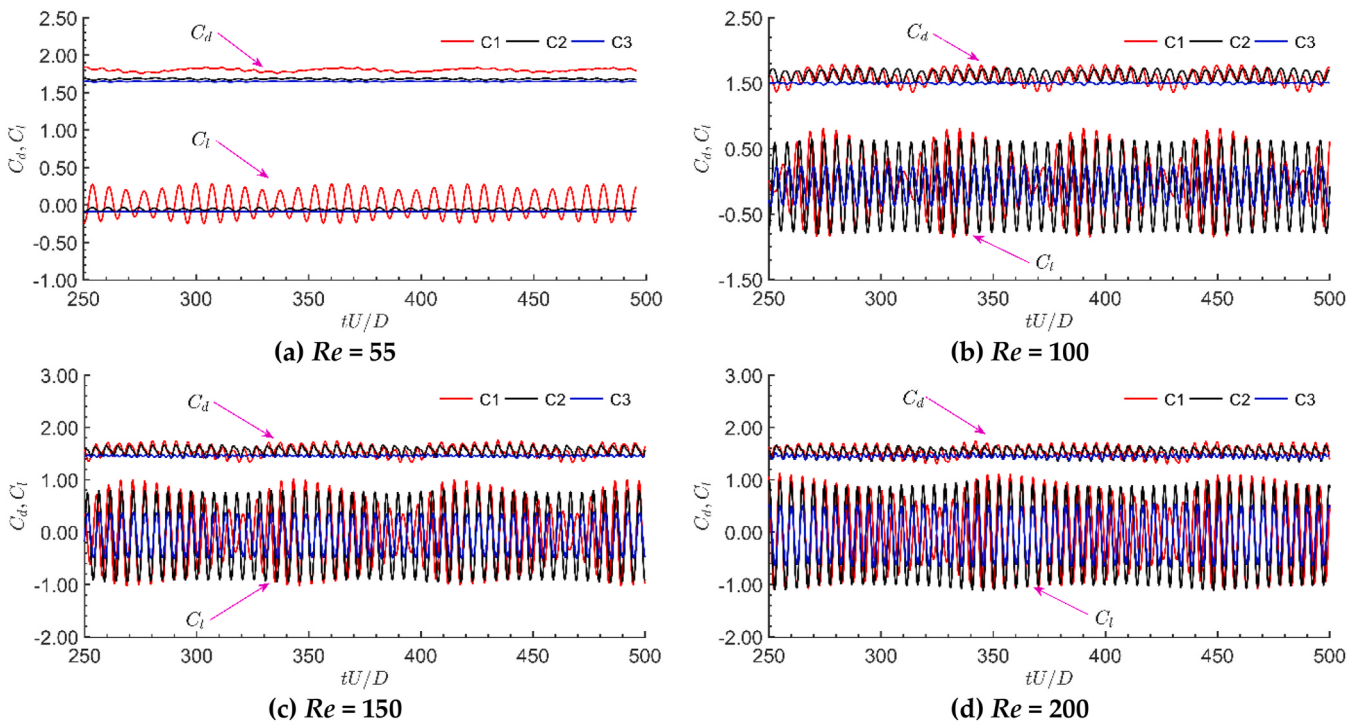
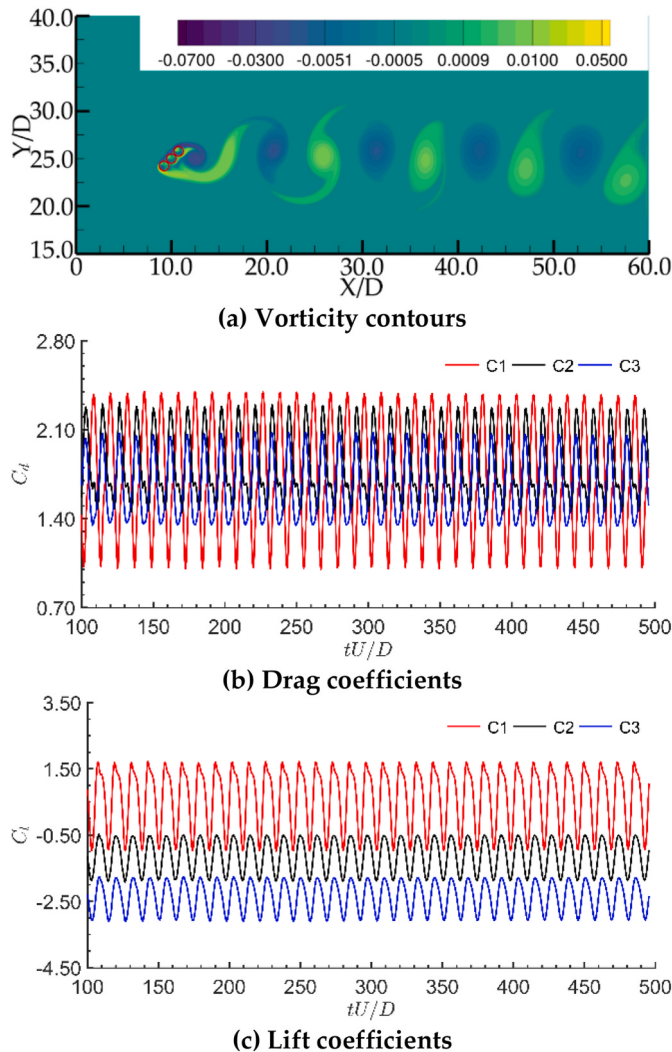


Fig. 12. Drag and lift coefficients for three cylinders in staggered arrangement ( $\delta = 3$ ,  $\theta = 45^\circ$ ).

three staggered arrangement cylinders with  $Re = 100$  and  $\theta = 45^\circ$  for  $\delta$  ranging from 0.1 to 8.0 are depicted in Fig. 13–18. In this section, four wake patterns are considered.

**4.1.2.1. Single bluff body wake pattern.** Single bluff-body wake flow mode for three cylinders in a staggered arrangement for  $\delta = 0.10$  and  $\theta = 45^\circ$  at  $Re = 100$  was observed in Fig. 13. It can be obtained from Fig. 13 (a) that the gap flow rate for  $\delta = 0.10$  is extremely small and cannot effectively interfere with the near wake of the cylinders, which

causes the inner vortex shedding at the gap sides to be completely suppressed. Vortex shedding occurred only at the freestream sides of the upper cylinder C1 and lower cylinder C3, which formed a single cylinder vortex pattern with a Karman vortex street phenomenon in the far-wake downstream region. Furthermore, it is obvious that the flow behavior for three cylinders in a staggered arrangement with a small gap ratio ( $\delta \leq 0.20$ ) closely resembles the flow pass through a single bluff cylinder but with an elongated recirculation bubble with augmented characteristic length. Although the gap flows among the three cylinders are very weak,



**Fig. 13.** Single bluff body pattern for three cylinders in staggered arrangement ( $Re = 100$ ,  $\theta = 45^\circ$ , and  $\delta = 0.10$ ).

they significantly influence the vortex shedding frequency, drag coefficient, and lift coefficient. Fig. 13 (b) and (c) show the change of the drag and lift coefficients over time history, and it can clearly be obtained that there is a regular and periodic characteristic of instantaneous drag and lift coefficient variations. The drag coefficients of C2 and C3 have in-phase fluctuations, which are anti-phase with C1, and the lift coefficients all have in-phase fluctuations among the three cylinders. Further, the lift force amplitude of C1 is larger than those of C2 and C3, which is since the downstream cylinder is in the wake influence area under the influence of gap flow. We also found that the dominant frequencies of the drag and lift coefficients are highly consistent, which supports the finding that three cylinders ( $\theta = 45^\circ$ ,  $\delta = 0.20$ ) behave like a single bluff cylinder. The critical gap ratio for the wake flow mode changing from single bluff cylinder wake mode to deflected wake mode is 0.20. The single bluff cylinder wake mode of flow pass through side-by-side or staggered circular cylinders was also observed by Aboueian and Sankar (2017), Supradeepan and Roy (2014), Adeeb et al. (2018), and Griffith et al. (2017). The single bluff cylinder wake mode for three or more cylinders with small gap ratio was also observed by Han et al. (2013), Kang (2003), Chen et al. (2020), and Ullah and Zhou (2020).

**4.1.2.2. Deflected wake pattern.** As the gap ratio increases to 0.30, the deflected wake pattern can be perceived at  $Re = 100$  in Fig. 14. Obviously, we can get that the inner vortex shedding from the gap side of the upper

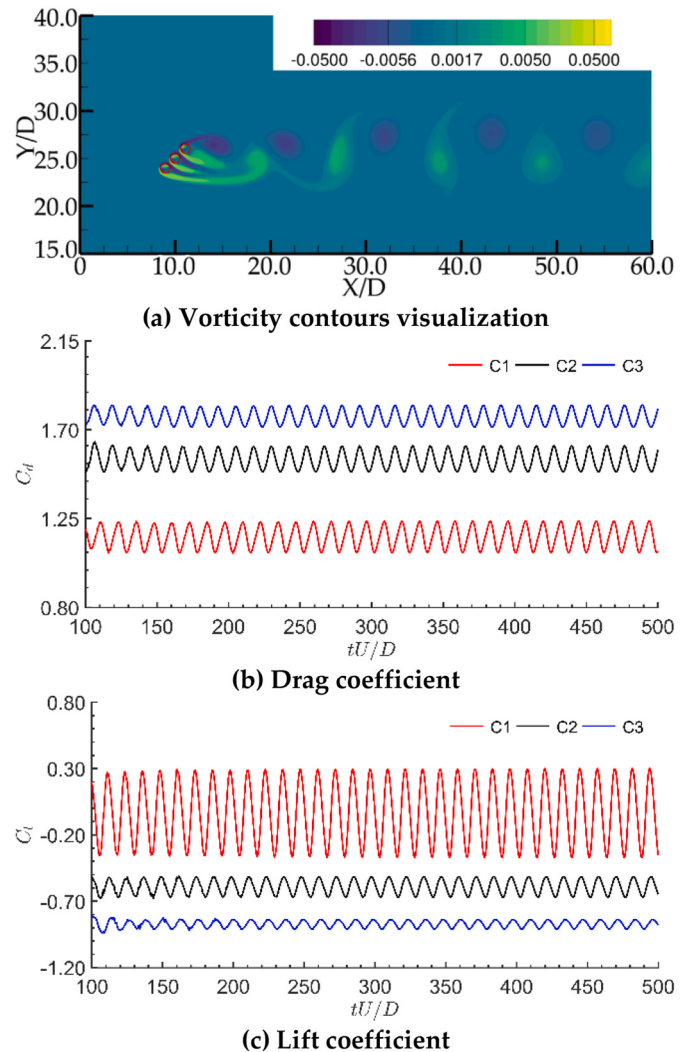


**Fig. 14.** Deflected wake pattern for three staggered arrangement cylinders in ( $Re = 100$ ,  $\theta = 45^\circ$ , and  $\delta = 0.50$ ).

cylinder C1 and lower cylinder C3, as well as the vortices shed from C2, are deflected towards one of the two vortices shedding from the freestream sides, and the deflection direction no longer changes. Furthermore, the gap flows are completely suppressed by the vortex shedding from the free-stream sides of upper cylinder C1 and lower cylinder C3, and a single-row vortex formed by the shear layer, which is composed of positive and negative augmented vortices, can be observed in the downstream flow. One interesting observation is that the free-side wake vortices of C3 are generated in the form of augmented and elongated bubble, as opposed to a round-shaped, and are much longer than normal, especially for the lower cylinder C3. Time trace analysis results for the drag coefficient and lift coefficient of three staggered arrangement cylinders for  $\theta = 45^\circ$  and  $\delta = 0.50$  at  $Re = 100$  are shown in Fig. 14 (b) and (c). It can clearly be obtained that the instantaneous drag coefficient and lift coefficient have the characteristics of periodicity and regularity, and the lift force amplitude of C1 is larger than those of C2 and C3, which is consistent with that of single bluff cylinder wake mode. This phenomenon can be accounted for that the internal vortex shed from the gap side being deflected towards to the downstream cylinder C1, which augments the force exerted by the flow on the upstream cylinder C3. The critical gap ratio for the flow pattern changing from deflected wake mode to flip-flopping wake flow mode is 0.80. The deflected wake pattern has also been observed for three circular cylinders arranged in side-by-side with a narrow gap spacing (Kang, 2003; Han et al., 2013).

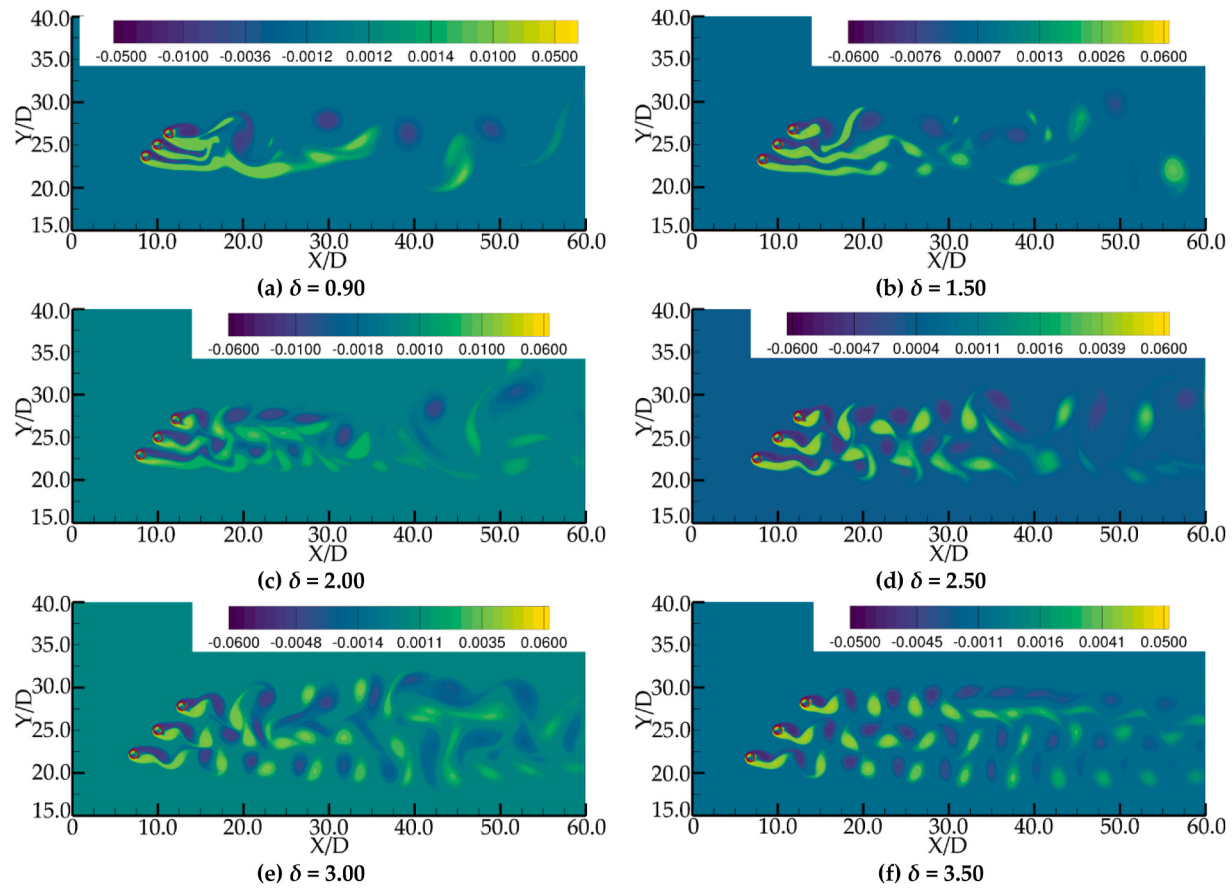


**Fig. 15.** Flip-flopping wake pattern behind three staggered arrangement cylinders ( $Re = 100$  and  $\theta = 45^\circ$ ).

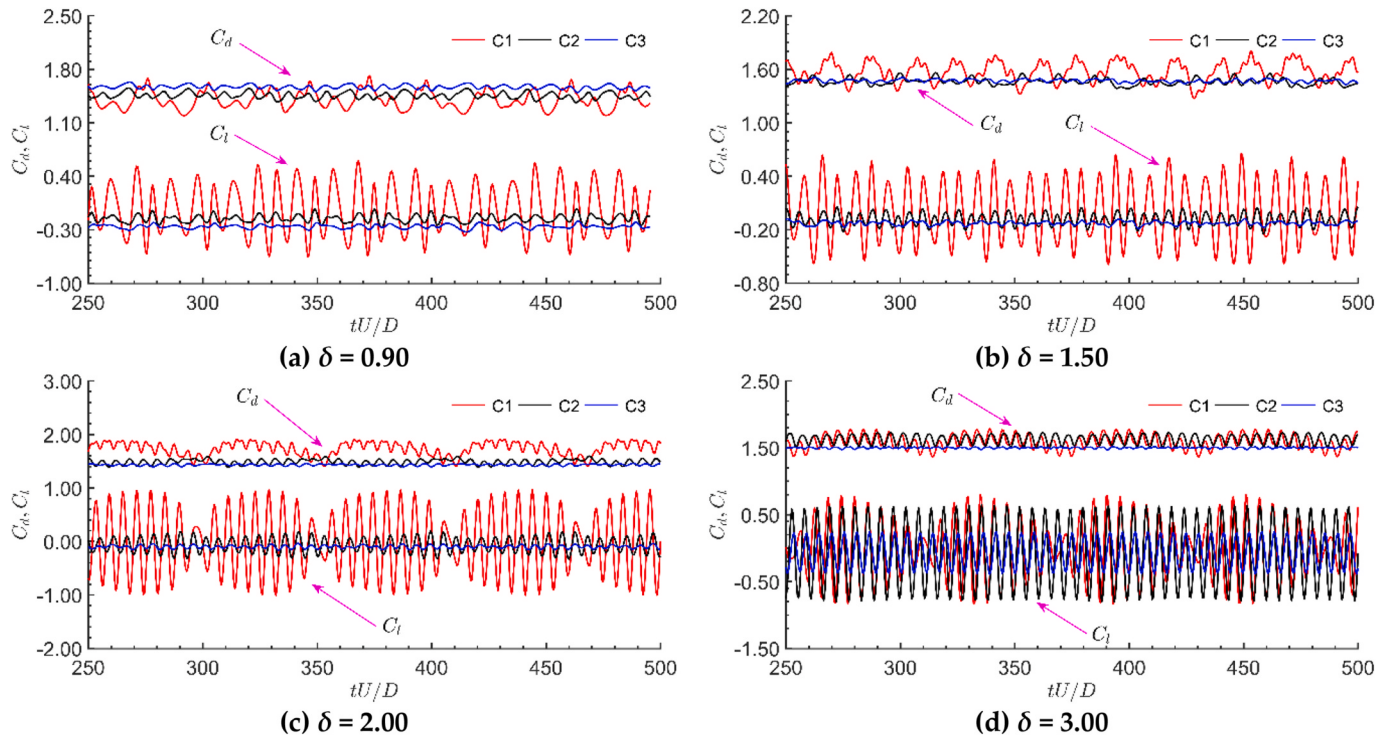


**Fig. 16.** Drag and lift coefficients for three staggered arrangement cylinders ( $\theta = 45^\circ$ ).

**4.1.2.3. Flip-flopping wake pattern.** Fig. 15 shows the vorticity contours for the flip-flopping flow structure, where the vortices generated in non-alternating manner in the downstream region. It is explicitly from Fig. 15 that the vortices in immediately downstream are not quite explicit; further, the vortices have strong mutual effects and are merged further downstream of the wake region. This phenomenon can be summarized as that the jet flow between the narrow gaps of consecutive cylinders is strong, which can be interpreted as the vortex shedding of the wake for the staggered arrangement with a larger gap becoming relatively complex, irregular, and arbitrary.

The time history of drag coefficient and lift coefficient for three staggered arrangement cylinders in flip-flopping wake flow pattern are shown in Fig. 16, where it is evident that the drag coefficient amplitude of C1 is more intricate and larger than those of C2 and C3, which can be interpreted as the flip-flopping wake pattern augmenting the forces exerted by C2 and C3 on C1. Furthermore, it is evident that the histories of  $C_d$  show more chaotic characteristics than those of  $C_l$ , and the characteristics of  $C_d$  and  $C_l$  are decoupled in this case. One interesting observation is that unlike the single bluff cylinder wake flow pattern and deflected wake flow pattern, a modulated-frequency sinusoidal variation pattern ( $\delta \geq 0.90$ ) based on the natural vortex shedding frequency and jet-induced frequency for both  $C_l$  and  $C_d$  is observed in the flip-flopping wake flow pattern. The modulation frequency first becomes obvious with an increase in the gap ratio  $\delta$  and then presents a decreasing trend. The critical gap ratio for the flow pattern to change from a flip-flopping wake pattern to a fully developed flow pattern is 3.50. In some literature, the flip-flopping wake flow pattern is also considered as chaotic flow pattern (Kang, 2003; Chatterjee et al., 2010). The flip-flopping wake flow mode was also observed by Chatterjee et al. (2010) for flow pass through five square cylinders arranged in side-by-side with a gap ratio of  $\delta = 1.2$ .

**4.1.2.4. Fully developed flow pattern.** As the gap ratio further increases, the interaction of vortices generated by different cylinders becomes weaker, and the vortices development process are more autonomic and independently (Adeeb et al., 2018). The wake pattern for the three cylinders in a staggered arrangement for  $Re = 100$  and  $\theta = 45^\circ$  was observed at  $\delta = 3.6, 5.0, 6.5$  and  $8.0$ , as shown in Fig. 17. It can obviously be observed that the single-body vortex wake pattern and Karman vortex street phenomenon are generated separately for the three individual cylinders. For  $\delta = 3.6$ , the vortices shed from middle cylinder C2

fluctuate and create a binary vortex street in the downstream region of the computational domain, then vortices are amalgamated weakly.

The time history of drag coefficient and lift coefficient for three staggered arrangement cylinders in flip-flopping wake flow pattern at  $\delta = 3.6, 5.0, 6.5$  and  $8.0$  are shown in Fig. 18. It can be seen that  $C_d$  and  $C_l$  are modulated periodically with different amplitudes, and the modulation frequency is relatively inconspicuous in comparison with the vortex shedding frequency; however, this modulation phenomenon essentially disappears at  $\delta = 8.0$ . The drag coefficient for C3 is greater than those of C1 and C2 in Fig. 18 (d), which may be caused by C3 being too close to the calculation boundary. We also observed that the effect of the gap distance almost disappears at  $\delta = 8.0$ , contrary to the observation in the case of  $\delta = 6.5$ ; similar results were reported by Zheng et al. (2016) and Bao et al. (2010).

#### 4.1.3. Flow pattern characteristics for three equilateral-triangular cylinders

Many scholars have deeply studied the flow around three cylinders in equilateral-triangular arrangement with different gap ratios and incident angles. The flow pattern characteristics are typically classified into three categories according to the gap ratio by Zdravkovich (1987), Gu and Sun (2001), Bao et al. (2010), and Zheng et al. (2016). Generally, the small gap, intermediate gap, and large gap are used to represent the proximity interference, combined interference, and wake interference, respectively.

**4.1.3.1. The small gap ratio.** The proximity effect plays a leading role in the flow pattern characteristics behind the equilateral-triangular cylinders with small gap ratios. Fig. 19 shows the flow and force characteristics of three equilateral-triangular cylinders for  $\delta = 0.4$  at  $Re = 100$ . According to the vorticity contours provided by Fig. 19 (a), it can be seen and observed that the shear layers, which generated from the free-stream-side surface of the upstream cylinder, enclosed the downstream side-by-side cylinder C2 and C3. The vortices generated from the gap side of the three cylinders are completely suppressed for that the gap flow is too weak to affect the wake regime. Thus, the flow pattern characteristics of three equilateral-triangular cylinders are consistent with those of a single bluff body. As Fig. 19 (b) shows, the biased flow, which is biased toward cylinder C2, is also observed behind the downstream cylinder C2 and C3. As illustrated in Fig. 19 (c)–(d), the instantaneous drag and lift coefficient varied periodically and regularly, and the amplitude of  $C_d$  and  $C_l$  of downstream cylinder C2 and C3 are

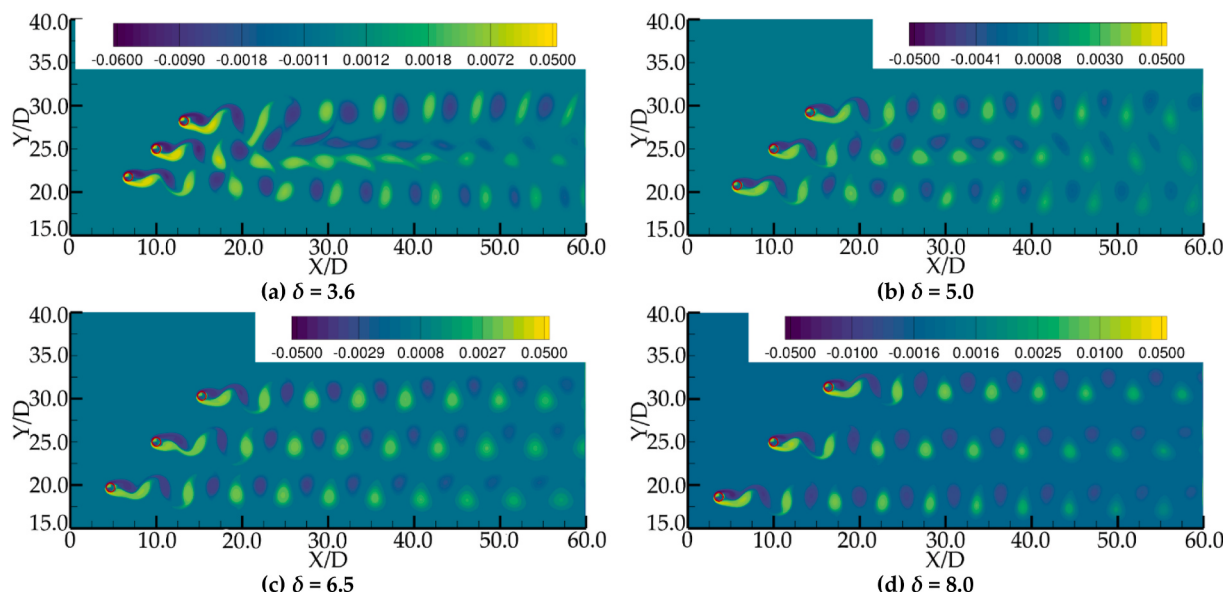


**Fig. 17.** Fully developed flow pattern behind three staggered arrangement cylinders ( $Re = 100$  and  $\theta = 45^\circ$ ).

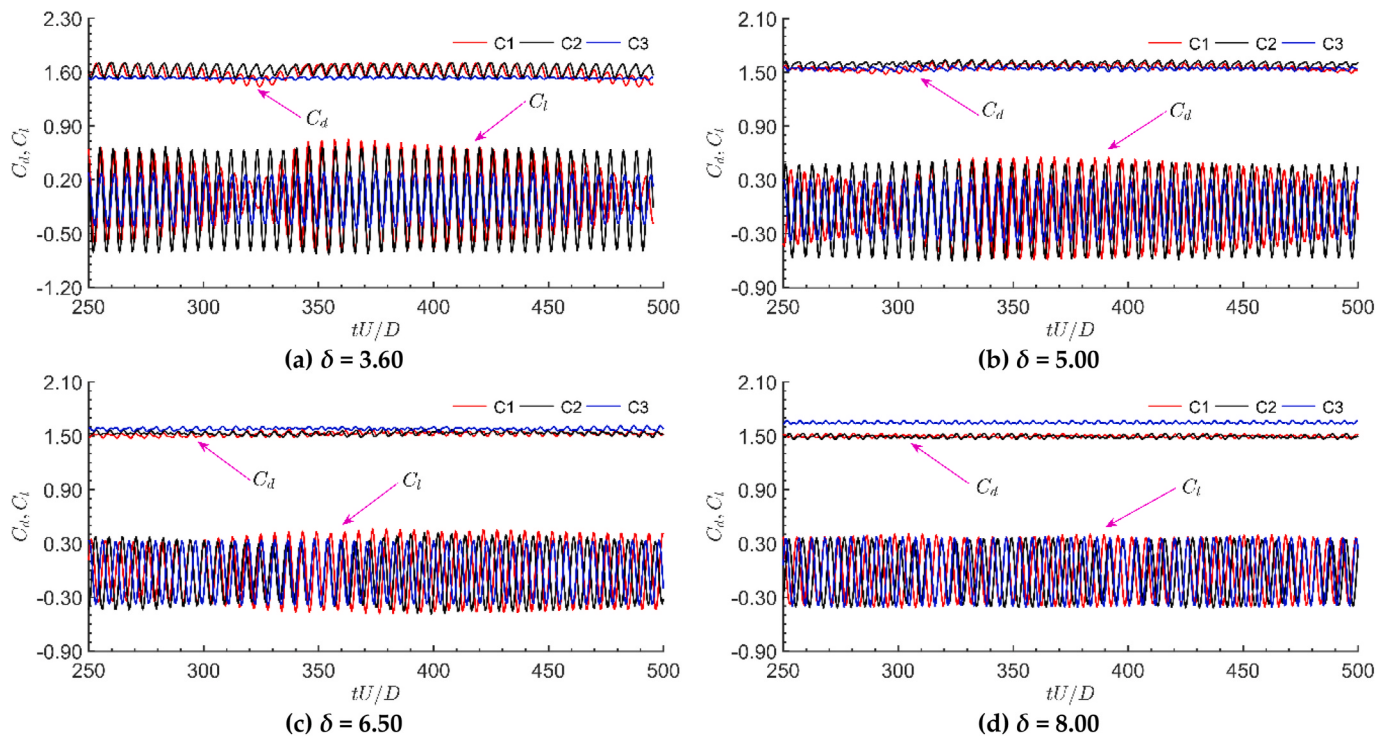


Fig. 18. Drag and lift coefficients for three staggered arrangement cylinders ( $Re = 100$  and  $\theta = 45^\circ$ ).

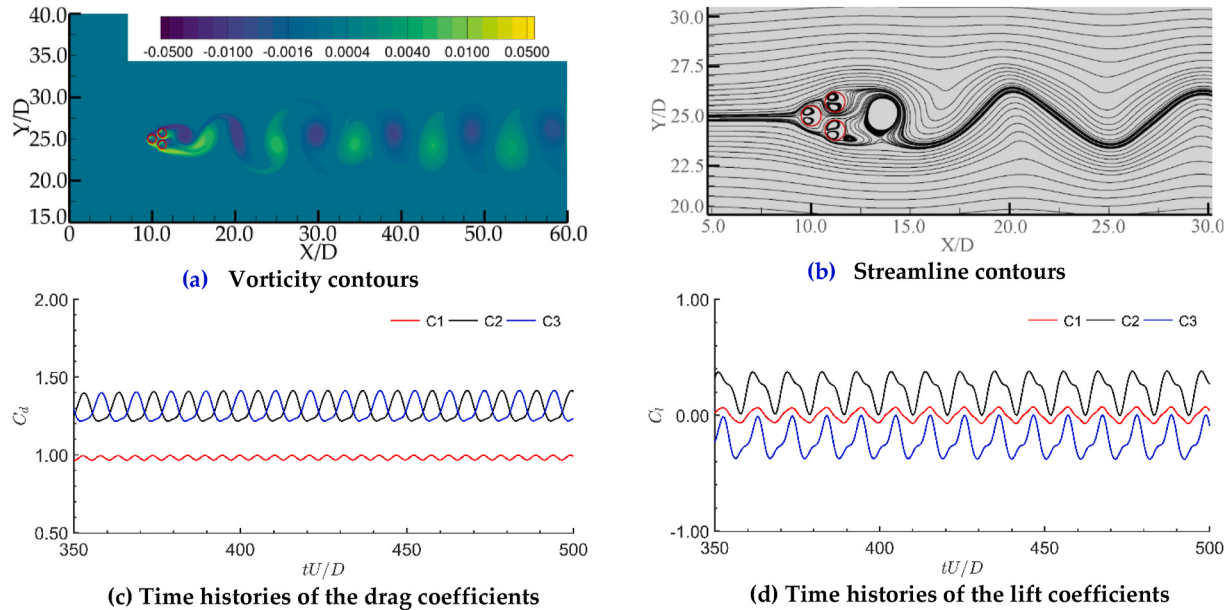


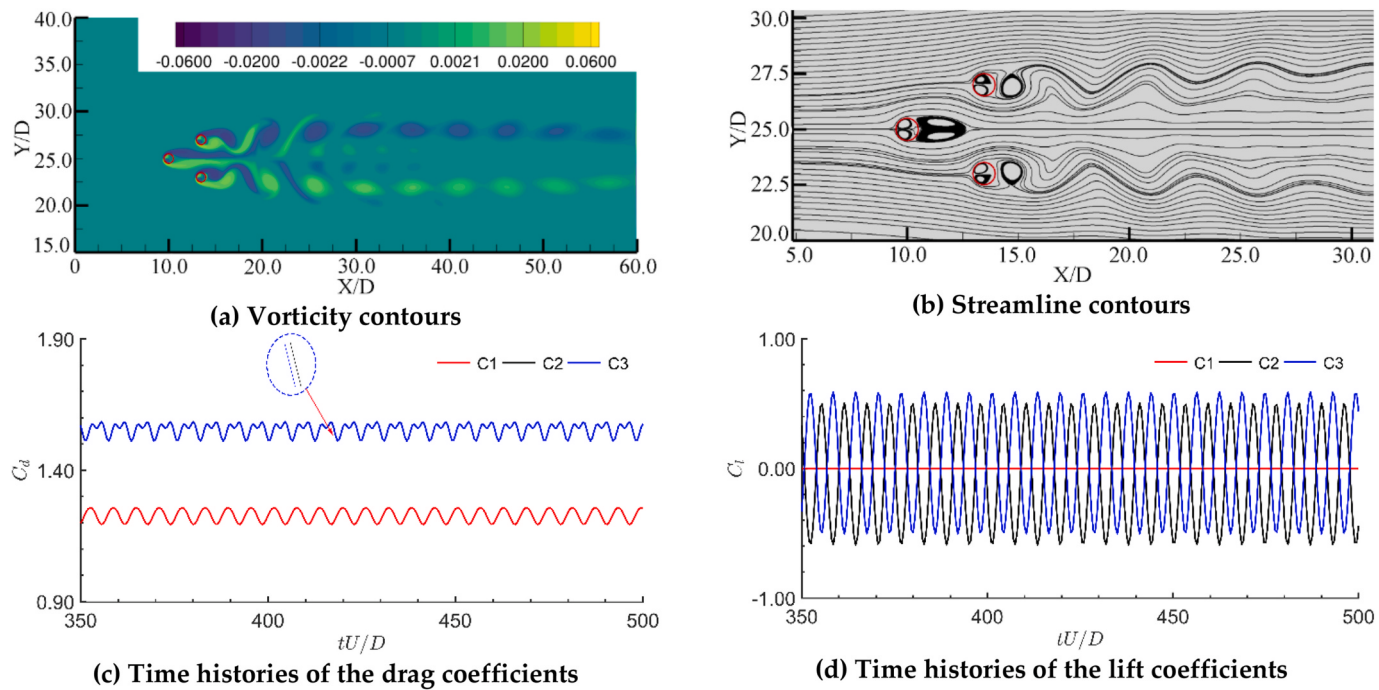
Fig. 19. Flow and force characteristics for  $\delta = 0.4$  at  $Re = 100$ .

significantly larger than that of upstream cylinder C1, which due to the fact that the vortices are mainly shed form the downstream cylinder rather than the upstream cylinder.

**4.1.3.2. The intermediate gap ratio.** The gap flow becomes more stronger as the increase of gap ratio, which weakened the proximity interference and improved the wake interference. The commingling of proximity interference and wake interference makes the flow pattern characteristics extremely complicated.

The flow and force characteristics for a typical combined interference for  $\delta = 3.0$  at  $Re = 100$ , was shown in Fig. 20. As can be seen from

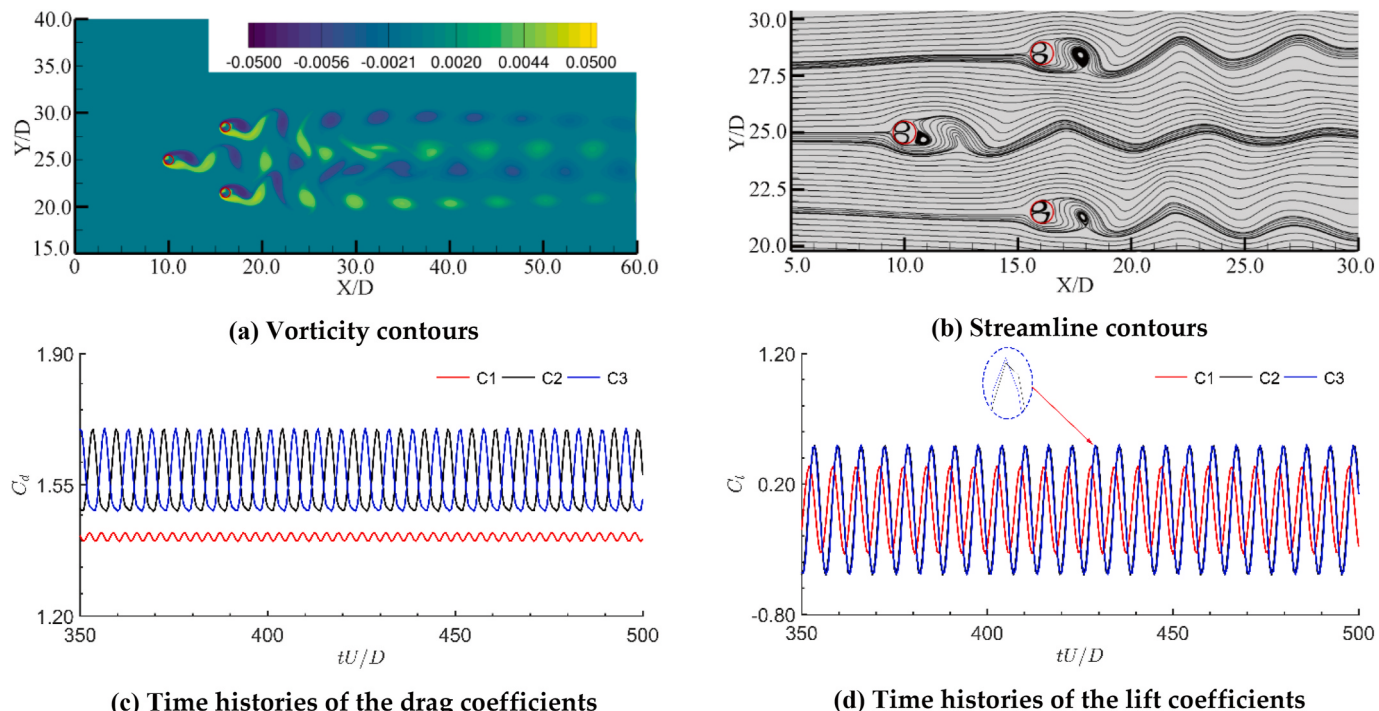
the Fig. 20 (a), the wake behind upstream cylinder C1 are sandwiched and stabilized by the downstream side-by-side cylinders, this stability also be confirmed by the fact that the lift coefficient equal to 0 for the upstream cylinder C1 (see Fig. 20d). It can also be observed that the vortex generated by the downstream side-by-side cylinders are anti-phase synchronized. In the streamline contours, there are two symmetric elongated recirculation bubbles with respect to the free stream direction developed behind the upstream cylinder C1, as shown in Fig. 20 (b). The time histories of drag and lift coefficient of three equilateral-triangular cylinders for  $\delta = 3.0$  at  $Re = 100$  were shown in Fig. 20 (c)–(d), it can be clearly observed from Fig. 20 (c) that the  $C_d$  of

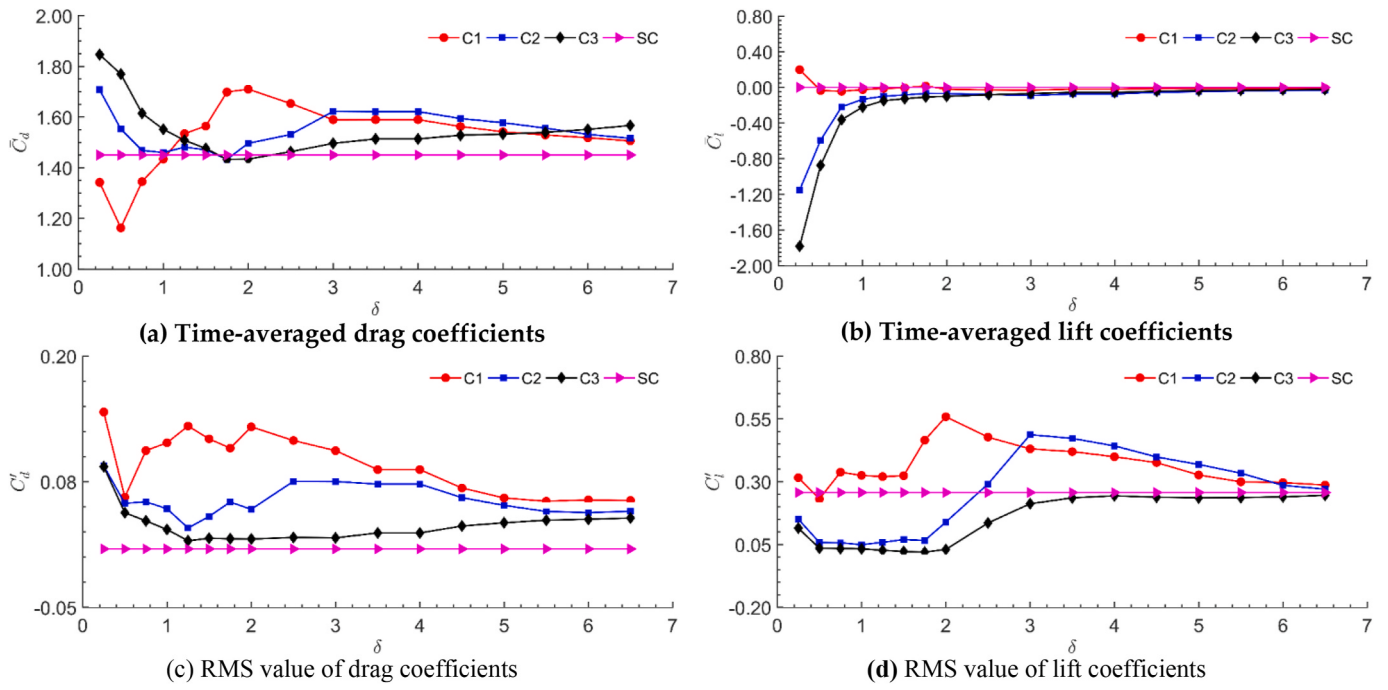
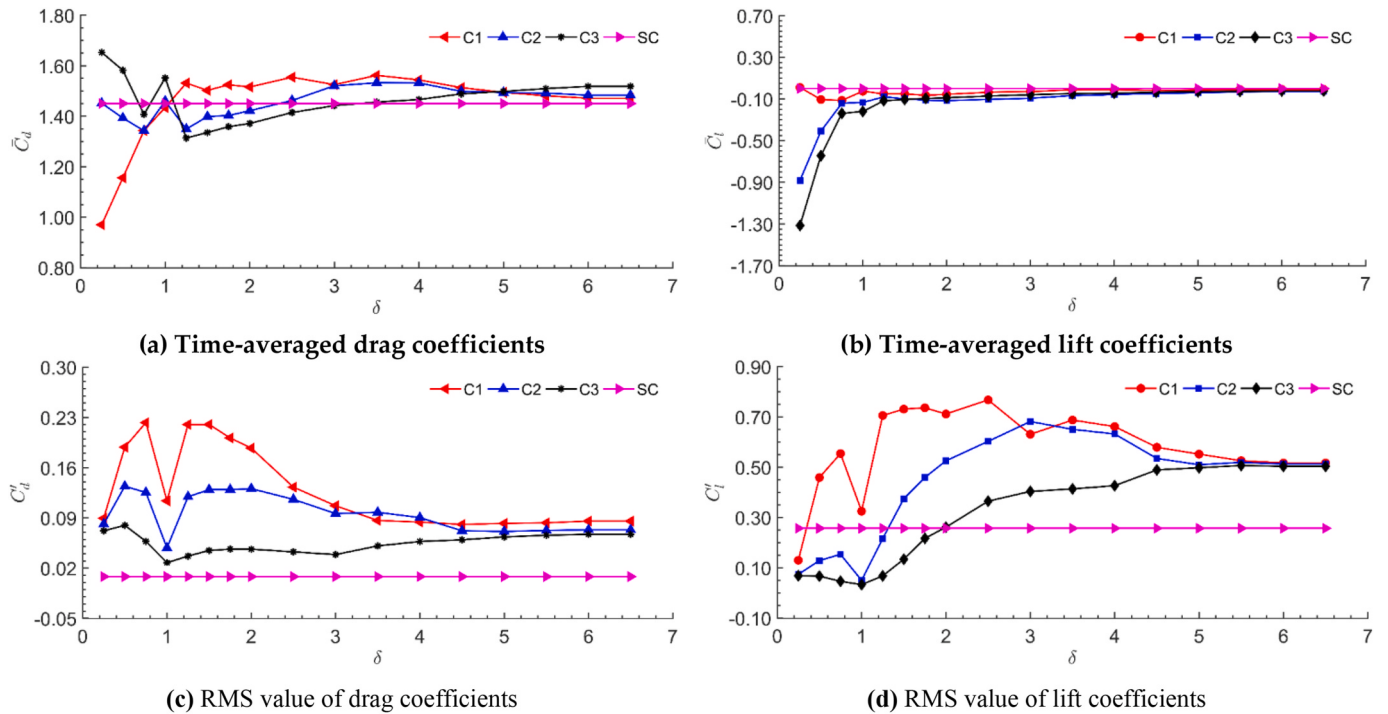
Fig. 20. Flow and force characteristics for  $\delta = 3.0$  at  $Re = 100$ .

downstream side-by-side cylinder is significantly higher than that of upstream. The Fig. 20 (d) illustrated that the  $C_l$  of upstream cylinder is a straight line, which suggest that the vortex generating from upstream cylinder is restrained by the downstream cylinders and maintained a steady state, while the  $C_l$  of downstream side-by-side cylinder changed in periodically sinusoidal function.

**4.1.3.3. The large gap ratio.** As the gap ratio increase to larger than 4, each cylinder would generate an independent fully developed vortex, the flow characteristics are mainly disturbed by the wake effect among three

cylinders rather than the gap ratio, and the wake flow effect also decreases with the increase of gap ratio. It can be obtained from Fig. 21 (a) that the vortices, shed from upstream cylinder C1, fluctuated in the area between the downstream cylinders, and the independent Karman vortex street phenomena can be observed at the wake of each cylinder. The  $C_d$  and  $C_l$  of each cylinder varied periodically and regularly with different amplitudes (Fig. 21c-d), It should be pointed out that the  $C_d$  and  $C_l$  amplitude of upstream cylinder C1 are smaller than those of downstream side-by-side cylinders, which due to that the downstream cylinders are in the wake influence area under the influence of upstream cylinder.

Fig. 21. Flow and force characteristics for  $\delta = 6.0$  at  $Re = 100$ .

Fig. 22. Variation of force coefficients with gap ratio at  $Re = 100$ .Fig. 23. Variation of force coefficients with gap ratio at  $Re = 200$ .

#### 4.2. Flow statistics

##### 4.2.1. Drag and lift coefficients

The variations in the time-averaged drag coefficient  $\bar{C}_d$  and lift coefficient  $\bar{C}_l$  of the three staggered arrangement cylinders with the gap spacing ( $\delta = P/D$ ) at  $Re = 100$  and 200 are shown in Fig. 22 and Fig. 23, respectively. Clearly,  $\bar{C}_d$  and  $\bar{C}_l$  depend mainly on  $\delta$  and are relatively insensitive to  $Re$ . It can be seen from Figs. 22(a) and Figure 23(a) that at a large gap ratio  $\delta$ ,  $\bar{C}_d$  for the three staggered arrangement cylinders case

is significantly greater than that of single cylinder case, this is consistent with the scientific observation of Zhou et al. (2021). It can be seen from Figs. 22(b) and Figure 23(b) that  $\bar{C}_l$  for all three cylinders significantly changes as  $\delta$  increases to 1 and then remains almost constant at zero at  $\delta > 2$ .  $\bar{C}_l$  for the three staggered arrangement cylinders case is in close proximity to that of single cylinder case. Figs. 22 and 23 also show that  $\bar{C}_d$  and  $\bar{C}_l$  for the three-cylinder case all approach the single-cylinder case with increasing  $\delta$ , which can be accounted for by the interaction among all three cylinders reducing with increasing  $\delta$ .

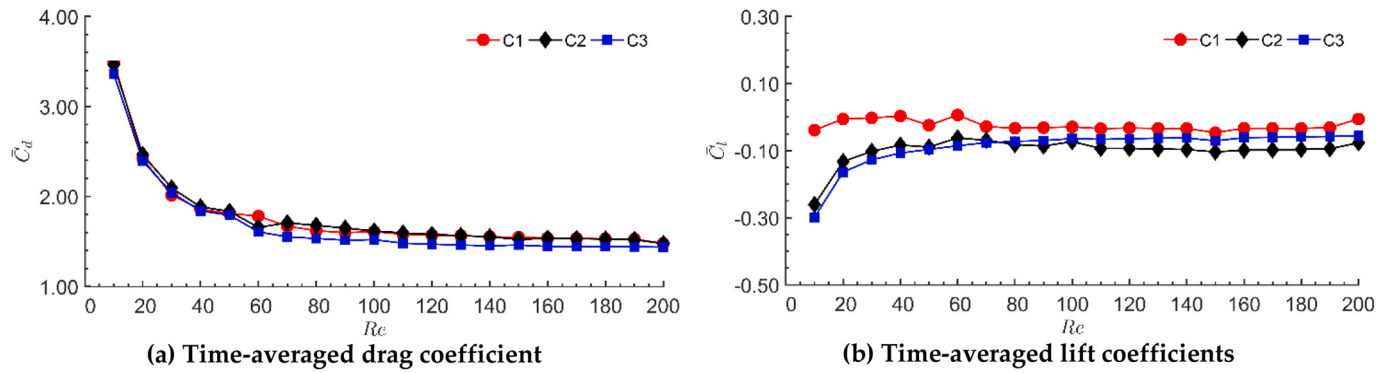


Fig. 24. Variation of force coefficients with gap ratio at different  $Re$  from 10 to 200.

The charts (c)–(d) of Figs. 22 and 23 show the variation of the RMS value for fluctuating drag coefficients and lift coefficients with gap ratio for  $Re = 100$  and 200. Fig. 23 (d) shown that the variation tendency of  $C'_d$  are increased first and then reached to the maximum, except for  $\delta = 1.0$  at  $Re = 200$ , which possibly due to the gap flow, and then decreased with the gap ratio increasing, and achieve a stable value at  $\delta = 6.0$ . The  $C'_l$  for three staggered cylinders are approximate to the value of a single cylinder at a larger gap for  $Re = 100$ . Further analysis showed that the variation tendency of  $C'_d$  and  $C'_l$  with gap ratio are basically similar for different  $Re$  number, but the  $C'_d$  and  $C'_l$  values are different, which suggest that the influence of gap flow on  $C_d$  and  $C_l$  also relates to  $Re$ .

Fig. 24 shows the variations of  $\bar{C}_d$  and  $\bar{C}_l$  with  $Re$   $\delta = 3.0$ . It can be observed that in the studied  $Re$  range, the value of  $\bar{C}_d$  shows a decreasing trend with  $Re$ , except at  $Re = 60$ . The deviation of  $\bar{C}_l$  from 0 indicates that there is mutual interference between the three cylinders in the flow field, which results in the asymmetry of the trailing vortex compared with that for a single cylinder.

#### 4.2.2. Strouhal number

The fast Fourier transform was used to calculate the frequency of vortex shedding around three cylinders in a staggered arrangement. Tu et al. (2020) noted that the peaks in the power spectral density (PSD) chart indicate the presence of flow interference. The PSD, which is normalized by  $f_s D/U$ , of the lift coefficient for three staggered arrangement cylinders with a gap ratio  $\delta = 0.25, 2.5$  and 5.0 are shown in Fig. 25. Here, the black, blue, and red curves denote cylinders C1, C2, and C3, respectively. It can clearly be seen from Fig. 25 that each PSD chart has at least one distinct peak frequency, which is called the Strouhal number. As described in Fig. 25 (a) and (d), one can see that the peak value of the three cylinders with small gap ratios ( $\delta = 0.25$ ) are consistent, which can be explained by the fact that the three cylinders behaved as a single bluff body under the condition of small gap ratios, it can also be observed that the main frequency value is about twice of the secondary frequency. It can be seen from Fig. 25 (c) and (e) that, for the flip-flopping wake pattern, the main frequencies are distributed over a broadband frequency range with no regularity, which can be interpreted as the vortex shedding for the staggered arrangement with intermediate gap ratio becoming relatively complex, irregular, and arbitrary. Fig. 25

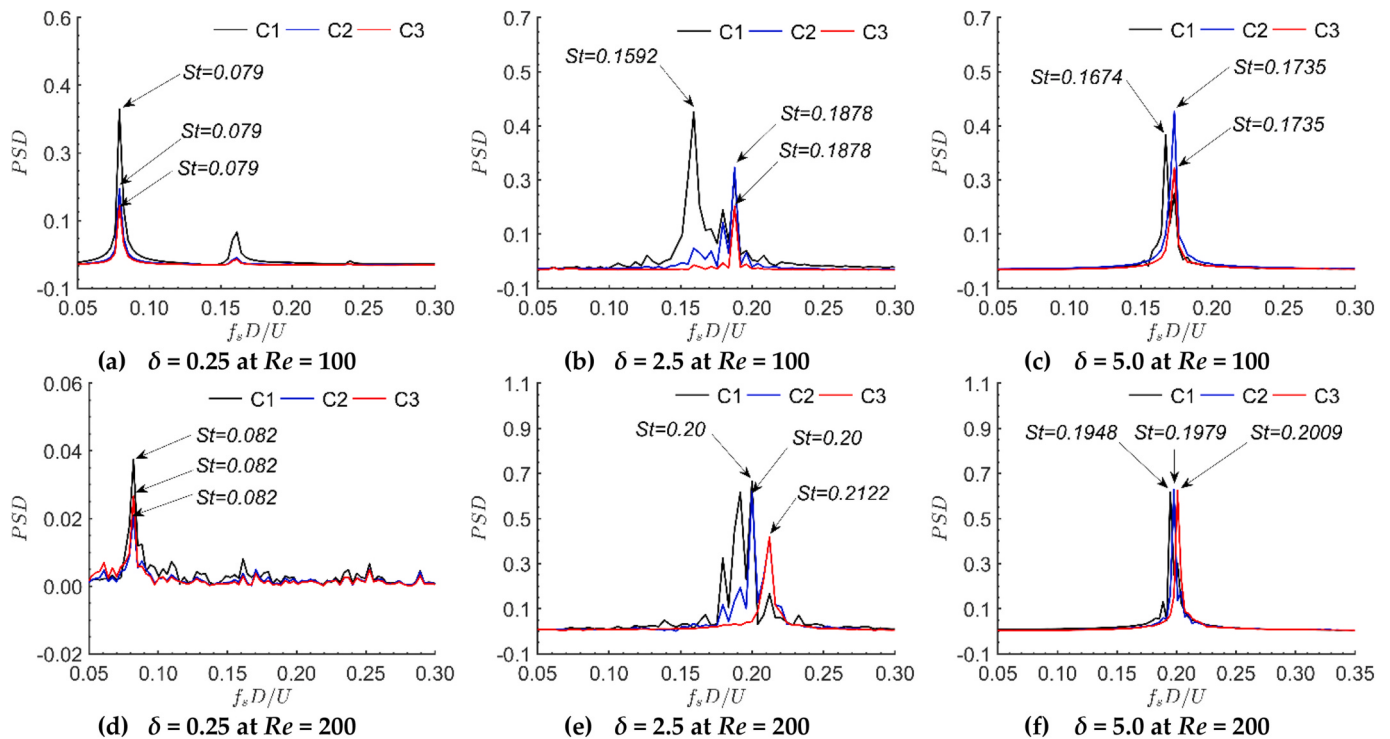


Fig. 25. Power spectral density of the lift coefficients.

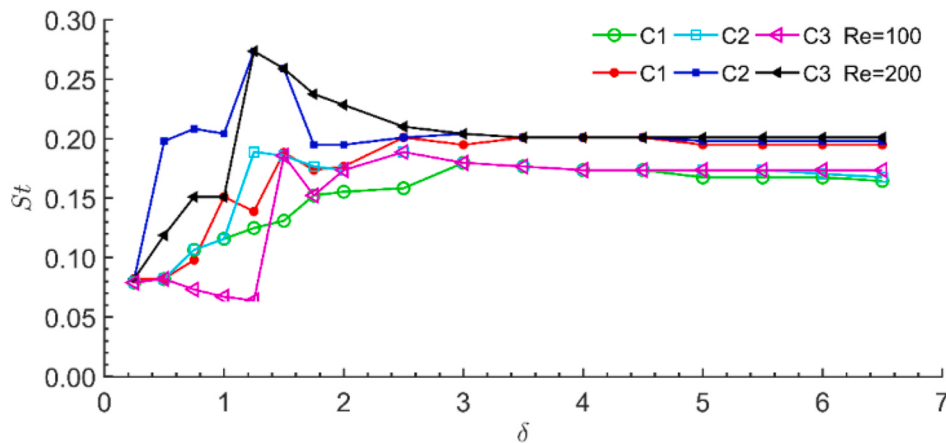


Fig. 26. Variation of  $St$  for three staggered cylinders with gap ratio at  $Re = 100$  and  $200$ .

(c) and (e) show that the  $St$  number of the three staggered cylinders with a large gap ratio ( $\delta = 6.0$ ) are almost the same, this phenomenon can be explained as that the wake flow effect is partially weakened with the increasing of gap ratio, and as the gap ratio equal to 6.0, each cylinder would generate an independent fully developed vortex. The same results have also been reported by Zhou et al. (2021), Tu et al. (2020) and Sewatkar et al. (2012) for multiple cylinders.

Fig. 26 shows the variation of  $St$  for three staggered cylinders with gap ratio for  $Re = 100$  and  $200$ . In the proximity regime with  $\delta = 0.25$ , the  $St$  of each cylinder is almost the same for that the three staggered cylinders behaved as a single bluff body. As the gap increases, the flow pattern changes from single bluff body wake pattern to flip-flopping wake pattern, all three cylinders have different  $St$  values because the vortex streets in the wakes of cylinder C1, C2, and C3 interacted with each other, especially for gap ratios of  $\delta = 0.75$  to  $3.0$ , further,  $St$  number shows more complex, irregular, and arbitrary, which is consistent with the irregularity of vortex shedding frequency. The  $St$  values are almost the same for large gap ratios ( $\delta > 3.5$ ), which can be explained by the fact that the interaction essentially disappears, and each cylinder would generate an independent fully developed vortex. It also can be obtained that the  $St$  values of the three staggered arrangement cylinders of large gap ratios at  $Re = 200$  are larger than those at  $Re = 100$ .

## 5. Conclusions

This study numerically investigated the flow pass through three circular cylinders at staggered and equilateral-triangle arrangement. The LBM was used to solve the fluid governing equations, and the IBM was adopted to resolve the fluid–structure interactions. Code correctness and grid independence were validated for two 2D cases, including an isolated cylinder and three tandem arrangement cylinders. The focus was on the effects of  $\delta$  and  $Re$  on the fluid dynamics, including wake patterns,  $C_d$ ,  $C_l$ , and the  $St$  of the fluid passing three cylinders. The main discoveries can be focused as follows:

- Depending on the gap ratio  $\delta$ , single bluff body, deflected, flip-flopping, and fully developed wake flow modes are observed for three staggered cylinders with incidence angle  $45^\circ$  at  $Re = 100$ , and the critical gap ratios for transitions among these are  $\delta \leq 0.2$ ,  $0.3 \leq \delta \leq 0.8$ ,  $0.9 \leq \delta \leq 3.5$ , and  $\delta \geq 3.6$ , respectively.
- The vortices shed from the three cylinders at staggered arrangement can be clearly observed for a gap ratio of  $\delta > 0.9$ . For a small gap ratio, the shed vortices in the downstream region are merged, and for large gap ratios, the independent vortex streets generate three cylinders without any merging in the downstream region.

- According to the gap ratio, the wake flow characteristics of flow around three cylinders arrayed in equilateral-triangle can be divided into proximity interference, combined interference, and wake interference.
- The  $C_d$  and  $C_l$  values of all three cylinders significantly changed as  $\delta$  increases to 1, but they remain almost constant at  $\delta > 2$ , and  $C_l$  for the three staggered arrangement cylinders is in close proximity to that of single-cylinder case. In the studied  $Re$  range, the value of  $C_d$  shows a decreasing trend with  $Re$ , except at  $Re = 60$ .
- The flow interference among three staggered arrangement cylinders is significant in the small-gap flow regime ( $\delta \leq 1.0$ ), while such an influence is partially weakened in the large-gap flow regime ( $\delta \geq 4.0$ ). All three cylinders have different  $St$  values, which becomes less obvious as the gap ratio increases.

## Funding

This work was supported by the National Natural Science Foundation of China (grant number 51975537, 52105283), Natural Science Foundation Key Projects of Zhejiang Province (grant number LZ22E060002) and Huzhou Public Welfare Application Research Project (grant number 2020GZ01).

## CRediT authorship contribution statement

Rongyang Wang: Data curation, Writing – original draft, Revised. Yanhu He: Formal analysis, Writing – original draft. Liqun Chen: Designed and performed the experiments. Yingpeng Zhu: Writing – review & editing. Yikun Wei: Conceptualization, Methodology.

## Declaration of competing interest

The authors declare that they have no known competing financial interests or personal relationships that could have appeared to influence the work reported in this paper.

## Acknowledgments

The authors greatly appreciate the valuable comments and suggestions provided by the pre-publication reviewers.

## References

- Abbasi, W.S., Islam, S.U., Lubna, F.A.I.Z., Rahman, H., 2018a. Numerical investigation of transitions in flow states and variation in aerodynamic forces for flow around square cylinders arranged inline. *Chin. J. Aeronaut.* 31 (11), 2111–2123.
- Abbasi, W.S., Islam, S.U., Rahman, H., Manzoor, R., 2018b. Numerical investigation of fluid-solid interaction for flow around three-square cylinders. *AIP Adv.* 8 (2), 025221.
- Aboueian, J., Sohankar, A., 2017. Identification of flow regimes around two staggered square cylinders by a numerical study. *Theor. Comput. Fluid Dynam.* 31 (3), 295–315.
- Adeeb, E., Haider, B.A., Sohn, C.H., 2018. Flow interference of two side-by-side square cylinders using IB-LBM—Effect of corner radius. *Results Phys.* 10, 256–263.
- Alam, M.M., Bai, H., Zhou, Y., 2016. The wake of two staggered square cylinders. *J. Fluid Mech.* 801, 475–507.
- Bai, X.D., Zhang, W., Wang, Y., 2020. Deflected oscillatory wake pattern behind two side-by-side circular cylinders. *Ocean Eng.* 197, 106847.
- Bao, Y., Zhou, D., Huang, C., 2010. Numerical simulation of flow over three circular cylinders in equilateral arrangements at low Reynolds number by a second-order characteristic-based split finite element method. *Comput. Fluids* 39 (5), 882–899.
- Chatterjee, D., Biswas, G., Amiroudine, S., 2010. Numerical simulation of flow past row of square cylinders for various separation ratios. *Comput. Fluids* 39 (1), 49–59.
- Chen, W., Ji, C., Xu, D., Zhang, Z., 2020. Oscillation regimes and mechanisms in the vortex-induced vibrations of three circular cylinders with equilateral-triangular arrangements. *Phys. Fluids* 32 (4), 043602.
- Cui, X., Yao, X., Wang, Z., Liu, M., 2017. A hybrid wavelet-based adaptive immersed boundary finite-difference lattice Boltzmann method for two-dimensional fluid–structure interaction. *J. Comput. Phys.* 333, 24–48, 2017.
- Dash, S.M., Lee, T.S., Huang, H., 2014. A novel flexible forcing hybrid IB-LBM scheme to simulate flow past circular cylinder[J]. *Int. J. Mod. Phys. C* 25 (1), 1340014.
- Deng, J., Ren, A.L., Zou, J.F., Shao, X.M., 2006. Three-dimensional flow around two circular cylinders in tandem arrangement. *Fluid Dynam. Res.* 38 (6), 386–404.
- Gao, Y., Qu, X., Zhao, M., Wang, L., 2019. Three-dimensional numerical simulation on flow past three circular cylinders in an equilateral-triangular arrangement. *Ocean Eng.* 189, 106375.
- Griffith, M.D., Jacono, D.L., Sheridan, J., Leontini, J.S., 2017. Flow-induced vibration of two cylinders in tandem and staggered arrangements. *J. Fluid Mech.* 833, 98–130.
- Gu, Z., Sun, T., 2001. Classifications of flow pattern on three circular cylinders in equilateral-triangular arrangements. *J. Wind Eng. Ind. Aerod.* 89 (6), 553–568.
- Han, Z., Zhou, D., Tu, J., 2013. Laminar flow patterns around three side-by-side arranged circular cylinders using semi-implicit three-step Taylor-characteristic-based-split (3-TCBS) algorithm. *Eng. Appl. Comp. Fluid* 7 (1), 1–12.
- Hu, J.C., Zhou, Y., 2008. Flow structure behind two staggered circular cylinders. Part 1. Downstream evolution and classification. *J. Fluid Mech.* 607, 51–80.
- Islam, S.U., Abbasi, W.S., Ying, Z.C., 2016. Transitions in the unsteady wakes and aerodynamic characteristics of the flow past three square cylinders aligned inline. *Aero. Sci. Technol.* 50, 96–111.
- Islam, S.U., Manzoor, R., Ying, Z.C., Islam, Z.U., 2018. Numerical investigation of different aspect ratios for flow past three inline rectangular cylinders. *J. Braz. Soc. Mech. Sci.* 40 (9), 1–19.
- Kang, S., 2003. Characteristics of flow over two circular cylinders in a side-by-side arrangement at low Reynolds numbers. *Phys. Fluids* 15 (9), 2486–2498.
- Kang, S.K., Hassan, Y.A., 2011. A comparative study of direct-forcing immersed boundary-lattice Boltzmann methods for stationary complex boundaries. *Int. J. Numer. Methods Fluid.* 66 (9), 1132–1158.
- Kim, J., Kim, D., Choi, H., 2001. An immersed-boundary finite-volume method for simulations of flow in complex geometries. *J. Comput. Phys.* 171 (1), 132–150.
- Lai, M.C., Peskin, C.S., 2000. An immersed boundary method with formal second-order accuracy and reduced numerical viscosity. *J. Comput. Phys.* 160 (2), 705–719.
- Ma, S., Kang, C.W., Lim, T.B.A., Wu, C.H., Tutty, O., 2017. Wake of two side-by-side square cylinders at low Reynolds numbers. *Phys. Fluids* 29 (3), 033604.
- Ma, L., Gao, Y., Guo, Z., Wang, L., 2018. Experimental investigation on flow past nine cylinders in a square configuration. *Fluid Dynam. Res.* 50 (2), 025504.
- Niu, X.D., Shu, C., Chew, Y.T., Peng, Y., 2006. A momentum exchange-based immersed boundary-lattice Boltzmann method for simulating incompressible viscous flows. *Phys. Lett.* 354 (3), 173–182.
- Qian, Y.H., d'Humières, D., Lallemand, P., 1992. Lattice BGK models for Navier-Stokes equation. *Europhys. Lett.* 17 (6), 479–484.
- Sewatkar, C.M., Patel, R., Sharma, A., Agrawal, A., 2012. Flow around six in-line square cylinders. *J. Fluid Mech.* 710, 195–233.
- Shui, Q., Duan, C., Wang, D., Gu, Z., 2021. New insights into numerical simulations of flow around two tandem square cylinders. *AIP Adv.* 11 (4), 045315.
- Supradeepan, K., Roy, A., 2014. Characterisation and analysis of flow over two side by side cylinders for different gaps at low Reynolds number: a numerical approach. *Phys. Fluids* 26 (6), 063602.
- Tu, J., Zhang, Z., Lv, H., Han, Z., Zhou, D., Yang, H., Fu, S., 2020. Influence of the center cylinder on the flow characteristics of four-and five-cylinder arrays at subcritical Reynolds number. *Ocean Eng.* 218, 108245.
- Ullah, N., Zhou, C.Y., 2020. Fluid dynamics of flow around side-by-side arranged cylinders. *Arabian J. Sci. Eng.* 45 (7), 5907–5923.
- Vasel-Be-Hagh, A.R., Ting, D., Carriveau, R., 2013. Correlating flow pattern with force coefficients in air flow past a tandem unit of three circular cylinders. *Int. J. Fluid Mech. Res.* 40 (3), 235–253.
- Wang, S.Y., Tian, F.B., Jia, L.B., Lu, X.Y., Yin, X.Z., 2010. Secondary vortex street in the wake of two tandem circular cylinders at low Reynolds number. *Phys. Rev. E* 81 (3), 036305.
- West, G.S., Apelt, C.J., 1997. Fluctuating lift and drag forces on finite lengths of a circular cylinder in the subcritical Reynolds number range. *J. Fluid Struct.* 11 (2), 135–158.
- Wu, J., Shu, C., 2009. Implicit velocity correction-based immersed boundary-lattice Boltzmann method and its applications. *J. Comput. Phys.* 228 (6), 1963–1979.
- Yang, Z., Wang, X., Si, J.H., Li, Y., 2020. Flow around three circular cylinders in equilateral-triangular arrangement. *Ocean Eng.* 215, 107838.
- Yuan, H.Z., Niu, X.D., Shu, S., Li, M., Yamaguchi, H., 2014. A momentum exchange-based immersed boundary-lattice Boltzmann method for simulating a flexible filament in an incompressible flow. *Comput. Math. Appl.* 67 (5), 1039–1056.
- Zdravkovich, M.M., 1987. The effects of interference between circular cylinders in cross flow. *J. Fluid Struct.* 1 (2), 239–261.
- Zheng, S., Zhang, W., Lv, X., 2016. Numerical simulation of cross-flow around three equal diameter cylinders in an equilateral-triangular configuration at low Reynolds numbers. *Comput. Fluids* 130, 94–108.
- Zhou, Y., Wang, Z., Qian, Y., Yang, H., Wei, Y., 2021. Numerical simulation of the flow around two square cylinders using the lattice Boltzmann method. *Phys. Fluids* 33 (3), 037110.